Journal of
Mechanics of
Materials and Structures

Ryan L. Holloman, Karthikeyan Kandan, Vikram Deshpande and Haydn N. G. Wadley

msp

DYNAMIC COMPRESSION OF SQUARE TUBE CELLULAR STRUCTURES

RYAN L. HOLLOMAN, KARTHIKEYAN KANDAN,
VIKRAM DESHPANDE AND HAYDN N. G. WADLEY

Aluminum cellular structures have been fabricated by combining a two-dimensional $[0°/90°]_2$ arrangement of square Al 6061-T6 alloy tubes with orthogonal tubes inserted in the out-of-plane direction. By varying the tube wall thickness, the resulting three-dimensional cellular structures had relative densities between 11 and 43%. The dynamic compressive response of the three-dimensional cellular structure, and the two-dimensional $[0°/90°]_2$ array and out-of-plane tubes from which they were constructed, have been investigated using a combination of instrumented Kolsky bar impact experiments, high-speed video imaging, and finite element analysis. We find the compression rate has no effect upon the strength for compression strain rates up to $2000 \, \text{s}^{-1}$, despite a transition to higher-order buckling modes at high strain rates. The study confirms that a synergistic interaction between the colinear aligned and out-of-plane tubes, observed during quasistatic loading, extends to the dynamic regime. Finite element simulations, using a rate-dependent, piecewise linear strain hardening model with a von Mises yield surface and an equivalent plastic strain failure criterion, successfully predicted the buckling response of the structures, and confirmed the absence of strain-rate hardening in the three-dimensional cellular structure. The simulations also reveal that the ratio of the impact to back-face stress increased with strain rate and relative density, a result with significant implications for shock-load mitigation applications of these structures.

1. Introduction

Light sandwich-panel structures are widely used in stiffness-governed design, where large bending stresses must be supported with minimum elastic deflection [Allen 1969]. Since the flexural modulus of a sandwich panel increases with the square of its core thickness, the primary purpose of the core is to maintain separation of the face sheets at minimum mass [Vinson 1999]. By combining carbon fiber-reinforced polymer composite face sheets with lightweight Nomex and other polymeric cores, very high-flexural modulus structures have been developed for a variety of applications [Shahdin et al. 2009]. Advances in fabrication methods have led to the emergence of sandwich panels whose faces and cellular cores are made from high-strength metallic alloys based upon aluminum [Kooistra et al. 2004; Queheillalt et al. 2008], stainless steels [Ferri et al. 2006; Radford et al. 2007], and titanium [Queheillalt et al. 2000; Elzey and Wadley 2001; Moongkhamklang and Wadley 2010]. These sandwich structures also have high flexural strengths and moduli, and offer significant advantages over monolithic plates of equivalent mass in a variety of dynamic loading scenarios [Xue and Hutchinson 2004; Deshpande and Fleck 2005; Dharmasena et al. 2009; 2013; Wadley et al. 2013].

The benefits of metallic sandwich structures during localized impulsive loading arise from their high flexural strength and significant plastic strain energy dissipation. Some of the incident kinetic energy

---

is stored as the plastic work of core compression, but for edge-clamped panels, a substantial fraction is also dissipated by plastic stretching of the core and face sheets [Zok et al. 2004]. Numerous cellular core topologies have been investigated for dynamic loading applications, including honeycombs with in-plane stretch-resistant square [Wadley et al. 2007] or triangular [Wei et al. 2008; Dharmasena et al. 2011] cells, as well as more-compressible prismatic topologies based upon corrugations (with stretch resistance in only one direction) [Rimoli et al. 2011]. Concepts such as flex honeycomb [Bitzer 1997, pp. 1–9] or lattice truss cores [Kooistra et al. 2008] have been proposed for curved sandwich panels, but these cores are significantly less stretch resistant.

The sandwich-panel approach is not widely used to mitigate automobile impacts. Instead this community has focused on crash box (tube) designs that absorb the kinetic energy during frontal vehicle impact [Hanssen et al. 2000b; 2001], and reduce force transmission to levels that remain below the injury threshold for vehicle occupants. An ideal crash box design provides close to theoretical plastic energy absorption at predictable (constant) force through progressive buckling and plastic deformation of the box/tube structure. However, the crush response of tubes is highly impact orientation-dependent [Abramowicz and Jones 1997; Pingle et al. 2011]. More-isotropic aluminum foams [Reyes 2008] and foam-filled tubes [Reid 1993; Baumeister et al. 1997; Hanssen et al. 2000a] have therefore received attention for these structural impact problems. These foam-based structures are highly compressible, and can undergo compression at nearly constant (plateau) stress to plastic strains of 60% or more, making them efficient impact energy absorbers. However, they possess little (or none) of the in-plane stretch resistance that is utilized in sandwich panel-based mitigation approaches.

The compressive stress versus strain response of cellular structures is frequently found to depend upon the rate of straining [Dannemann and Lankford 2000; Deshpande and Fleck 2000]. This can arise from material strain-rate hardening [Wadley et al. 2003], changes in the deformation modes of the cells [Maiti et al. 1984] and from inertial effects [Calladine and English 1984]. To eventually design a structure whose energy absorption and stress transfer are insensitive to the rate or direction of compression, it is necessary to understand the significance of each of these factors to the overall response. The objective of the study reported here is to investigate the dynamic crushing of a cellular structure made from a three-dimensional arrangement of square cross section, extruded tubes of a heat-treatable 6061 aluminum alloy, shown in Figure 1(a), that exhibits negligible strain-rate hardening. The structure contains $[0°/90°]_2$ oriented in-plane tubes that provide in-plane stretch resistance, while the through-thickness tubes resist compression in analogous fashion to that of a crash box design.

A recent study of the quasistatic compressive response of three-dimensional tube structures [Holloman et al. 2013] revealed a synergistic interaction between the in and out-of-plane tubes that enhanced the energy dissipated by the structure's component tubes. The compressive energy absorption was comparable to that of axially loaded tubes, but had superior stretch resistance [loc. cit.], and a more omnidirectional crush response than a collinear tube array. The study also showed that by using different wall thicknesses for the in-plane and through-thickness tubes, it was possible to independently control the in-plane stretch resistance and the through-thickness crush strength. The large nodal contact areas also improved load transfer within the core, and between the core and face sheets. The topology also afforded multifunctionality [Evans et al. 2001] such as cross-flow heat exchange via the open channels that extend within the structure [Tian et al. 2007]. The study described here investigates the dynamic out-of-plane compressive response of the same structures. The dynamic crushing resistance and collapse mode mechanisms are
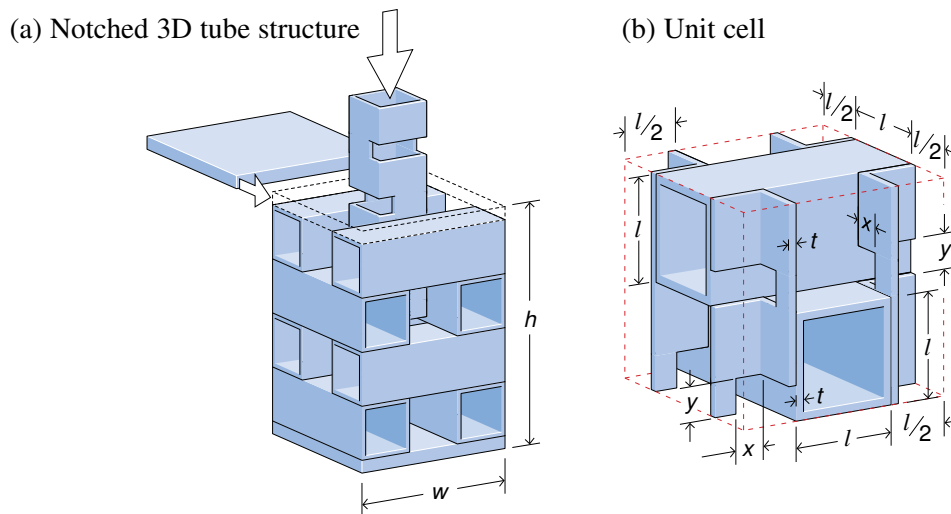
Figure 1. (a) A three-dimensional tube structure with the vertical tube notched to facilitate dip braze bonding. (b) The unit cell of the three-dimensional structure with the notch geometry incorporated. For all experiments reported here, $x = y = 6.35$ mm.

explored via direct-impact Kolsky bar experiments that utilize high-speed photography. Finite-element analysis is also used to investigate the dynamic deformation modes, and to estimate the stresses at the impact and distal faces of the structures.

2. Experimental protocols

2.1. *Test structures.* A two-dimensional structure was first assembled by laying down a colinear layer of 6061 aluminum alloy square tubes, each spaced a tube width apart. A second, similarly spaced, layer was then orthogonally placed on the first, and the assembly sequence repeated to create a $[0°/90°]_2$ structure. The three-dimensional topology, shown in Figure 1(a), was then assembled from the two-dimensional structure by inserting additional tubes in the out-of-plane (vertical) void space between the cross-ply oriented tubes. The out-of-plane tube was notched, as shown in Figure 1(a), to facilitate complete fluid penetration during subsequent dip brazing bonding and heat treatment [Holloman et al. 2013]. Since the notches affect the buckling response, additional three-dimensional samples were fabricated using regular out-of-plane tubes without notches. Samples consisting of just the regular and notched vertical tubes (called one-dimensional structures here) were also fabricated and tested. Following the dip brazing process, all the structures were slow-aged at room temperature for 96 hours to the T4 condition and then peak hardened (to the T6 condition) by heating to 163° C for 18 hours, followed by water quenching. Figure 1(a) shows that when the cellular tube structures are bonded to 4.76 mm thick face sheets to create sandwich panels, they have a large core-to-face-sheet interfacial area with potentially beneficial consequences for the robustness of intensely loaded panels. The structure's relative density, $\bar{\rho}$, given by the ratio of the volume occupied by metal to that of a unit cell — see Figure 1(b) — was calculated for each sample. A summary of the geometries and relative densities of the samples investigated is presented in Table 1.

| Topology | Sample core | | In-plane | | Out-of-plane | | |
	w (mm)	h (mm)	t (mm)*	l (mm)*	t (mm)*	l (mm)*	$\bar{\rho}$
1D	19.1	76.2	–	–	1.52	19.1	6.7**
2D	57.2	76.2	1.70	19.1	–	–	16.3
3D	57.2	76.2	1.45	19.1	1.45	19.1	20.1
3D	34.4	55.4	0.74	11.5	0.74	11.5	11.6
3D	57.2	76.2	3.47	19.1	3.47	19.1	42.7
1D unnotched	19.1	76.2	–	–	1.52	19.1	7.3**
3D unnotched	57.2	76.2	1.44	19.1	1.44	19.1	21.0

* Variability in the tube wall thickness resulted in reporting a mean value per sample with a standard deviation in tube wall thickness of ± 0.14 mm.

** Corresponds to relative density contribution to the three-dimensional structure.

Table 1. Tube core geometries (sample core widths and heights, w and h, and mean tube wall thicknesses, t, and tube widths, l) and relative densities ($\bar{\rho}$).

Tensile tests were previously performed on the tube wall alloy in postbrazed and peak-hardened condition [Holloman et al. 2013]. The experimental curve (measured at 25° C with a strain rate of $10^{-4}\,\mathrm{s}^{-1}$) is shown in Figure 2, and is later used to deduce the coefficients for a constitutive model for numerical simulation of the tube structures.
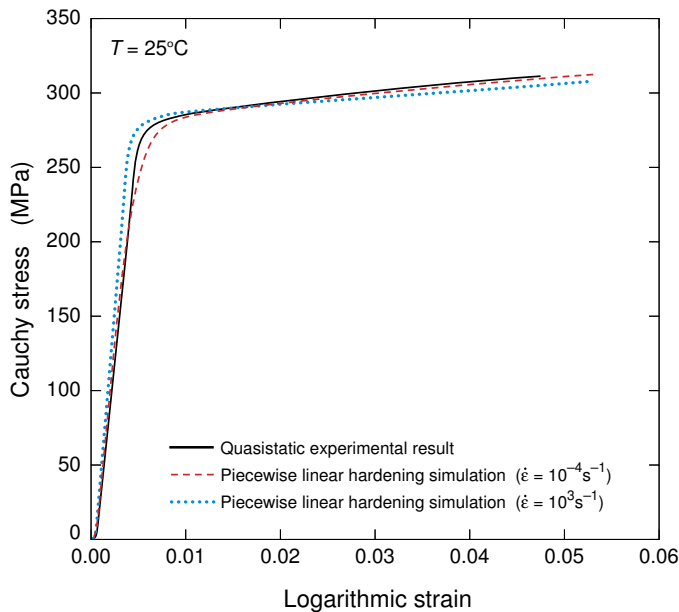

Figure 2. Measured tensile stress-strain relation for a sample of the 6061-T6 alloy extracted from a tube structure. The predicted responses of the constitutive model for strain rates of 10^{-4} and $10^3\,\mathrm{s}^{-1}$ are also shown.

2.2. *Dynamic testing.* The dynamic out-of-plane compressive response of the core structures was measured from a series of direct-impact Kolsky bar tests, where the force was measured on the sample's back face with a strain-gauged Kolsky [1949] bar while synchronously recording the strain with a high-speed video camera; see Figure 3. Each specimen was attached to the end of a stationary 2 m long, 7.62 cm diameter Kolsky bar using Loctite Super Glue. A striker projectile was accelerated with a gas gun towards the front face of the specimen, and the force transmitted by the sample was measured by diametrically opposed strain gauges placed 0.76 m from the impact end of the Kolsky bar. The striker diameter was equal to both the inner diameter of the gas gun barrel and the diameter of the Kolsky bar. The gas gun barrel measured 4.50 m in length; to achieve an impact velocity, v_0, of less than or equal to 75 ms^{-1}, the projectile was positioned 3.2 m from the exit of the barrel. Higher velocities were achieved by placing the striker projectile 3.8 m from the gun barrel exit. All initial velocities were measured near the barrel exit using two sets of laser velocity gates as shown in Figure 3. That figure also defines all other relevant geometrical parameters of the test setup. The Kolsky bar was made from aluminum alloy 6082-T6, with yield strength 310 MPa and measured longitudinal elastic wave speed $c = 5108$ ms^{-1}. A time window of 485.5 μs was therefore available for measurements before elastic reflections from the distal end of the Kolsky bar complicated interpretation.

The precision of the measurements was derived from multiple calibration tests. An example of one of the results is shown in Figure 4(a). The aluminum Kolsky bar was impacted by an aluminum projectile that had a diameter of 7.6 cm, a length of 54.0 cm, and a mass of 6124 g. In this example, it impacted the Kolsky bar with an initial (preimpact) velocity $v_0 = 7.3$ ms^{-1}. Figure 4(a) sets time $t = 0$ as the first arrival of the stress pulse at the strain gauges, and shows that the rise time of the stress pulse at the gauge location was 35 μs for the bar/strain gauge system used here. This rise-time limitation only became significant at the highest impact velocities, where substantial specimen compression could occur within the first 5 μs after impact.
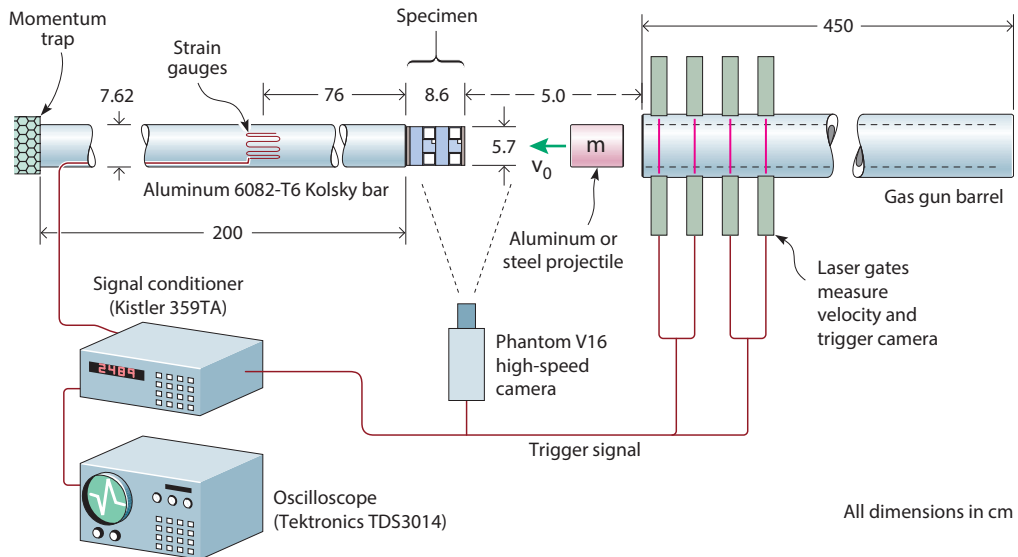

Figure 3. Schematic diagram of the Kolsky bar arrangement used for dynamic testing.
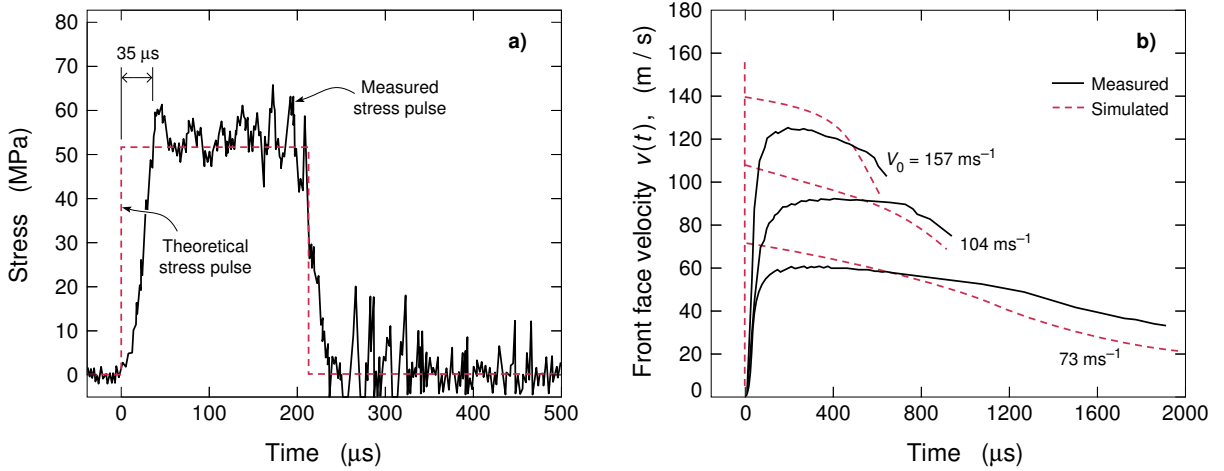
Figure 4. (a) Transmitted stress versus time history of the aluminum Kolsky bar following impact by a 54.0 cm long, 7.6 cm diameter aluminum striker with a mass of 6.124 kg and velocity $v_0 = 7.3 \, \mathrm{ms}^{-1}$. The axial stress in the aluminum Kolsky bar (predicted by one-dimensional elastic wave theory) was 51.3 MPa (the dashed curve). (b) The measured front-face velocity for a three-dimensional tube structure with $\bar{\rho} = 20.1\%$. Simulated data is also shown.

Elastic wave theory [Johnson 1972] gives the axial stress transferred to the aluminum Kolsky bar in this test as $\rho c v_0 / 2 = 51.3$ MPa, where $\rho = 2755 \, \mathrm{kg \cdot m^{-3}}$ is the density and $c = 5108 \, \mathrm{ms}^{-1}$ is the extensional wave speed of the aluminum Kolsky bar. The predicted axial stress pulse — the red dotted curve in Figure 4(a) — is within 16% of the first stress measured peak (61.2 MPa), and is reasonably close to the average measured stress. The measured calibration test stress drops to zero at $t = 236 \, \mu s$, which corresponds to the arrival of the elastic stress pulse reflected from the free end of the striker.

Russell et al. [2010] have shown that the striker projectile kinetic energy governs the compressive strain of the crushable sample and the transient velocity imposed upon the impacted end of the specimen. For the samples tested here, impact experiments were performed at nominal impact velocities of 75, 100, and 150 ms^{-1}. A steel striker of mass $M = 2.5$ kg was used for impact velocities v_0 of 75 and 100 ms^{-1}. It imparted sufficient momentum to crush most of the samples beyond their densification strain. An aluminum striker of mass $M = 0.75$ kg was used for tests at impact velocity $v_0 \geq 150 \, \mathrm{ms}^{-1}$. High-speed video images of the samples were recorded using a Phantom V12 high-speed camera to measure the compression rate, to identify failure modes and to confirm that the striker kinetic energy was sufficient to provide a constant-velocity sample compression up to a nominal strain of at least 50%. Figure 4(b) shows a typical impact face velocity result for a three-dimensional structure with $\bar{\rho} = 20.1\%$; the front-face velocity rose quickly upon striker impact to a peak crushing velocity and then fell slowly during continued crushing. The actual crush velocity was always slightly less than that of the striker just prior to impact, and remained relatively constant during crushing to the densification strain. As the relative density was increased to $\bar{\rho} = 42.7\%$, constant velocity compression ceased at core compressions of 20% and the samples were not completely crushed even with the more-massive striker. In the results to follow, we designate each test by the incident impact velocity, v_0, of the striker.

3. Finite element analysis protocols

Finite element (FE) techniques have been used to study the dynamic compression of one-, two-, and three-dimensional tubes. The aims of this aspect of the investigation were to

  (i) validate the analysis method by comparing the predicted and measured dynamic crush resistance of the tube structures,

 (ii) investigate the dynamic collapse mechanisms responsible for the mechanical responses of the cellular tube structures,

(iii) determine the stresses imposed on the front (not experimentally measured), and

(iv) rationalize the absence of strain rate strengthening of the structure.

3.1. *The FE model.* All the tests were analyzed using finite element simulations conducted using the explicit version of the commercial, nonlinear finite element package IMPETUS Afea Solver® [Hanssen and Olovsson 2013]. The geometry and relative density of the modeled tube specimens were designed to be the same as those of the measured specimens, reported in Table 1, but following the usual practice [Zok et al. 2005; Radford et al. 2007; Fyllingen et al. 2010], small imperfections (described below) were incorporated in the models to account for manufacturing defects, such as tube misalignment and tube wall thickness variability, seen in the tested specimens. The modeled sandwich structure geometry was merged with a modeled Kolsky bar of the same dimensions and with strain gauge placement as shown in Figure 3. The Kolsky bar model included a cylindrical gridded region, at the same location as the experimental strain gauges, where the axial displacements and forces could be inferred.

The FE models were constructed using cubic hexahedral elements. The meshing specifics are summarized in Table 2. A mesh sensitivity study indicated that an in-plane nodal spacing approximately equal to the tube wall thickness (t) was sufficient to provide converged solutions for impacts with tube core structures. One cubic hexahedral element was therefore used through the thickness of each tube wall. The nodes of the adjacent tubes were merged prior to the simulation, thus representing a perfect braze zone with no interface failure criterion [Holloman et al. 2013]. The contact formulation in the software is based on a penalty formulation. Simulations with uniform-wall-thickness models resulted in higher strengths than observed experimentally, and so imperfections to the geometries were introduced to trip buckling and better predict the stress-strain curves. The imperfections were modeled as a displacement of the lowest-order measured eigenmode to each tube wall. For most modeled structures the first-order eigenmode amplitude was set at 0.1 times the tube wall thickness; however, the unnotched tube structure required a larger amplitude imperfection (0.3 the tube wall thickness) to match the experiments.

All the simulations introduced a cylindrical projectile with the same dimensions and mass as the experimental projectile. An initial velocity (v_0) was applied to the simulated projectile that matched the measured projectile velocity recorded by the laser gates in the experiment. Conservation of momentum during the inelastic collision between the projectile and the specimen resulted in a decrease in projectile velocity, as shown in Figure 4(b).

3.2. *Material properties.* The experimentally recovered Cauchy stress-true strain response of the Al 6061-T6 alloy during uniaxial tensile testing is presented in Figure 2. The uniaxial Cauchy stress, σ,

Topology	$\bar{\rho}$	Hexahedral elements		Nodes
		Cubic	Linear	
1D	6.7	2,176	–	88,958
2D	16.3	5,440	–	297,854
3D	20.1	7,264	–	403,838
3D	11.6	5,356	1,936	345,958
3D	42.7	4,592	–	253,294
1D, unnotched	7.3	450	–	28,192
3D, unnotched	21.0	2,240	450	205,376

Table 2. Tube geometries and velocity-time function values used during FE simulations.

versus true strain, ε, relation for an elastic-plastic material under uniaxial straining can be written

$$\varepsilon = \varepsilon_e + \varepsilon_p = \frac{\sigma}{E} + \varepsilon_p, \tag{1}$$

where ε_e and ε_p are the elastic and plastic components of the strain, respectively, and E is the Young's modulus. Having performed the uniaxial tensile test, the true stress versus plastic strain curve was tabulated and used to determine an isotropic strain hardening relation needed for FE simulations. The transition from elastic to plastic behavior was set at a Cauchy stress of 230.7 MPa. This hardening tabulation was implemented in the IMPETUS Afea Solver using the general piecewise linear hardening constitutive model with optional thermal softening and strain-rate hardening. The yield stress of this model is defined in the form

$$\sigma_y = f(\varepsilon_{\mathrm{eff}})\left(1 - \left(\frac{T - T_0}{T_m - T_0}\right)^m\right)\left(1 + \frac{\dot{\varepsilon}_{\mathrm{eff}}}{\dot{\varepsilon}_0}\right)^c, \tag{2}$$

where $f(\varepsilon_{\mathrm{eff}})$ is the piecewise-linear hardening function of the effective deviatoric strain, which was obtained from the hardening curve behavior. The thermal softening component was defined by the current temperature, T, the reference temperature, T_0, the melting temperature, T_m, and the thermal softening parameter, m. The strain-rate hardening component of (2) was defined by a reference strain rate, $\dot{\varepsilon}_0$, and a strain-rate hardening parameter, c. The coefficients used in conjunction with (2) to model the material are given in Table 3. The thermal softening and strain-rate hardening components made a negligible contribution to the yield stress. The yield strength was primarily defined by the piecewise linear hardening function $f(\varepsilon_{\mathrm{eff}})$ modeled using a von Mises yield criterion with isotropic hardening. Using the material model described above, a uniaxial tensile test was simulated at room temperature for the measured strain rate and compared well to the measured Cauchy stress-logarithmic strain curve (Figure 2). The response at a strain rate of $10^3 \, \mathrm{s}^{-1}$ is also shown, and confirms the modest strain-rate dependence of the alloy.

To account for softening created by tube wall fracture on the tensile side of severely buckled tubes, the Cockcroft–Latham failure criterion [Cockcroft and Latham 1968] was implemented for all the dynamic compression simulations. Failure was defined to occur when a damage parameter, D, reached unity. The damage parameter was calculated as

$$D = \frac{1}{W_c} \int_0^{\varepsilon_{\mathrm{eff}}} \max(0, \sigma_1) \, d\varepsilon_{\mathrm{eff}}, \tag{3}$$

Elastic constant and density			Strain rate hardening		Temperature softening and adiabatic heating			Fracture parameter
E (GPa)	ν	ρ (kg·m^{-3})	ε_0 (s^{-1})	c	T_0 (K)	T_m (K)	m	W_c (MPa)
70.5	0.3	2700	$5 \cdot 10^{-4}$	0.001	293	893	1	85

Table 3. Material constants for AA6061-T6 tube wall material.

where σ_1 is the first principle stress. The critical damage parameter, $W_c = 85$ MPa, was obtained by fitting the simulated measured stress-strain response of a single laterally compressed tube tested in [Holloman et al. 2013]. The general node-splitting feature in the IMPETUS code was turned on. In this feature the damage variable is allowed to evolve without any change to the constitutive response of the Al 6061-T6 alloy until $D = 1$. At that instant, the Al 6061-T6 alloy is assumed to have failed and nodes of the elements where this failure has occurred are split apart.

4. Quasistatic core response

The quasistatic compressive responses of all the core structures investigated here have been investigated previously in [Holloman et al. 2013], and the key findings relevant to this study are summarized in Table 4, together with a summary of the dynamic results presented below. The relative density given to the one-dimensional tube samples corresponds to their contribution in a three-dimensional structure, Table 1. The compressive strengths of the one-dimensional (notched) and two-dimensional cores were 4.7 and 13.2 MPa, respectively. The addition of one and two-dimensional strengths (17.9 MPa) was less than the measured peak strength of the equivalent three-dimensional structure (20.8 MPa) with a relative density, $\bar{\rho} = 20.1\%$, indicating a substantial synergistic interaction between the colinear and vertical tubes during quasistatic loading. However, the mechanism responsible for the enhanced crush resistance of the fully integrated three-dimensional structure was not identified.

The volumetric energy absorption up to the core densification strain (ε_D) per unit volume,[1] E_v, and gravimetric energy absorption, $E_m = E_v / \bar{\rho} \rho_s$ (where r_s is the density of the aluminum alloy), are also given for each core in Table 4. The theoretical gravimetric energy absorption, E_m^* (the product of the compressive strength and densification strain divided by $\bar{\rho} \rho_s$), and the gravimetric energy-absorbing efficiency (E_m / E_m^*) are also summarized in Table 4. The energy-absorbing efficiency of the two-dimensional structures was low as a result of the unstable buckling response of the structure, making the two-dimensional core poorly suited for impact energy-absorption applications. All other structures exhibited energy-absorbed-per-unit-mass values near the upper bound for tubes [Holloman et al. 2013].

5. Dynamic compression results

We begin by examining the dynamic compression of the components (single-axial and two-dimensional tube arrays) of the three-dimensional cellular structure, and then investigate the fully integrated structure at three relative densities. Finite element analysis is used to resolve the tube collapse modes, identify the mechanism responsible for the synergistic effect, and estimate the impact-face pressure.

---

[1]Defined as the area under the stress strain response until the onset of densification.

Topology	$\bar{\rho}$	v (ms^{-1})	σ_p (MPa)	ε_D	E_v (MJ/m^3)	E_m (J/g)	E_m^* (J/g)	E_m/E_m^*
1D notched tube	6.7	0	4.7	0.72	1.7	9.4	18.7	0.50
		72	2.6	0.65	1.0	5.5	9.2	0.59
		105	3.2	0.56	1.4	7.7	9.6	0.80
		157	3.0	0.68	2.3	12.7	10.9	1.16
1D tube	7.3	0	10.3	0.79	5.3	26.9	39.6	0.68
		73	10.2	0.77	1.9	9.6	37.2	0.26
		108	11.6	0.75	3.3	16.7	40.8	0.41
		157	11.2	0.72	4.3	21.8	37.1	0.58
2D [0/90°]$_2$	16.3	0	13.2	0.64	1.2	2.7	19.2	0.14
		73	15.4	0.62	2.8	6.4	21.2	0.30
		104	13.4	0.59	4.3	9.7	17.3	0.56
		156	13.5	0.59	4.8	10.9	17.0	0.64
3D cellular structure	20.1	0	20.8	0.61	10.4	19.2	23.4	0.82
		73	18.2	0.59	8.4	15.5	18.2	0.85
		104	17.5	0.56	9.3	17.1	17.0	1.00
		157	17.2	0.56	8.8	16.2	16.6	0.98
3D cellular structure (unnotched)	21.0	0	27.1	0.63	12.5	22.0	30.1	0.73
		74	24.6	0.72	10.8	19.0	30.7	0.62
		108	21.8	0.66	10.5	18.5	24.5	0.75
		154	19.5	0.63	9.6	16.9	20.7	0.82
3D cellular structure	11.6	0	7.3	0.59	3.9	12.7	13.7	0.92
		72	7.0	0.73	2.8	8.9	16.3	0.55
		156	7.1	0.73	3.5	11.2	16.5	0.68
3D cellular structure	42.7	0	49.8	0.45	24.4	21.2	29.4	0.73
		73	53.2	–	–	–	–	–
		105	51.4	–	–	–	–	–
		157	56.6	–	–	–	–	–

Table 4. Measured mechanical properties (including relative density, $\bar{\rho}$, impact velocity, v, and compressive strength, σ_p) and energy absorption values (including volumetric energy absorption, E_v, gravimetric energy absorption, E_m, theoretical gravimetric energy absorption, E_m^*, and energy absorption efficiency, E_m/E_m^*) for tested tubular cellular structures.

5.1. *Axially loaded tubes.*

5.1.1. *Notched tube response.* The back-face pressure versus core strain responses of notched tubes impacted at the three velocities are given in Figure 5(b–d), and compared with the quasistatic result in Figure 5(a). The core strain, ε_c, for the impacted samples was defined as $\varepsilon_c = h^{-1}\int_0^t v(t)\,dt$, where $v(t)$ was the measured sandwich-panel impact-face velocity as a function of time t (measured from
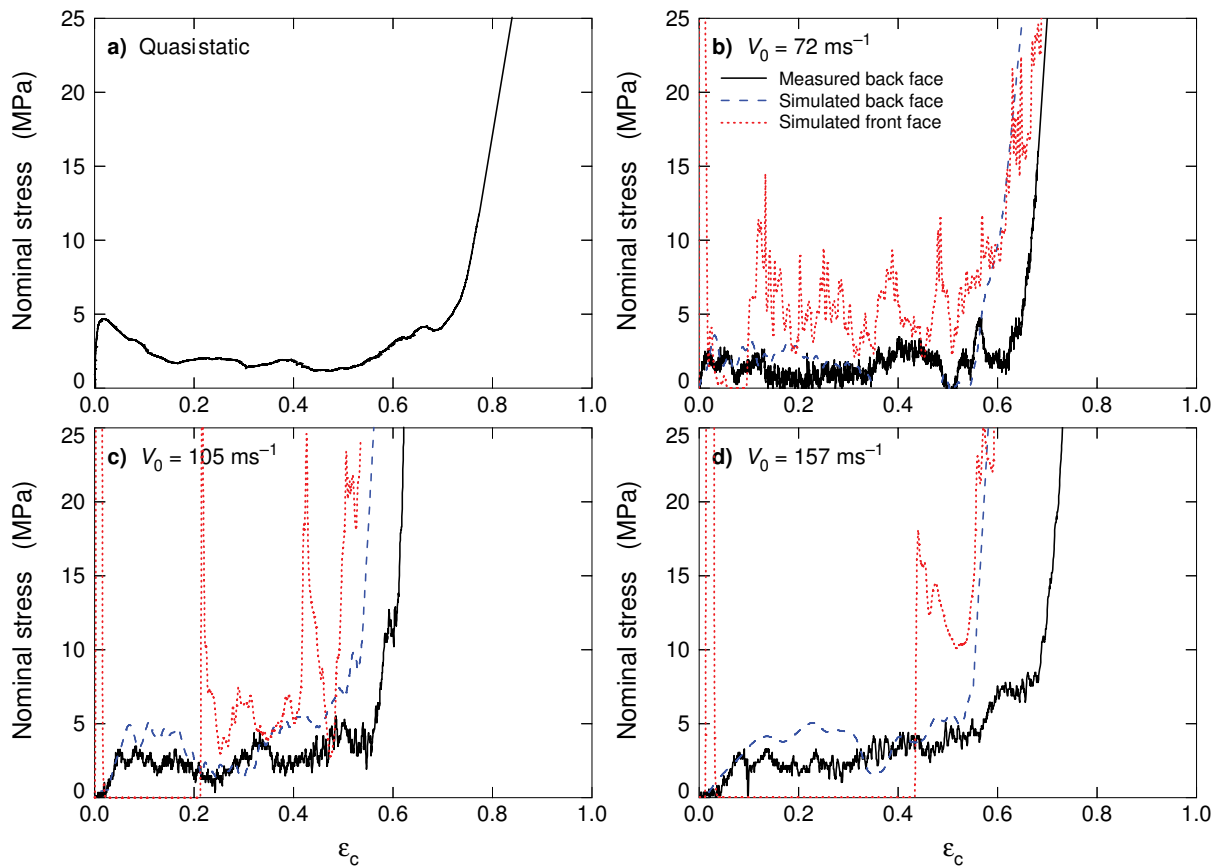
Figure 5. The measured and simulated back-face stress versus nominal compressive strain for a notched (one-dimensional) tube which contributed 6.7% to the relative density of a three-dimensional structure. (a) The quasistatic compression response followed by the responses after impact at (b) $72 \, \text{ms}^{-1}$, (c) $105 \, \text{ms}^{-1}$, and (d) $157 \, \text{ms}^{-1}$. Simulation results are also shown for the specimens' front (impacted) face pressure.

the high-speed photographs), and h the initial core height (85.7 mm). The predicted back-face stress versus imposed nominal strain results are overlaid on the experimental data in Figure 5, and found to be in good agreement with the measured back-face stress. Under quasistatic loading, examination of Figure 5(a) shows a plateau-like stress versus strain response after an initial peak in compressive stress of $\sigma_p = 4.7$ MPa. During dynamic impact at $72 \, \text{ms}^{-1}$ the stress-strain response remained plateau-like, as seen in Figure 5(b), but with a smaller initial stress peak of 2.9 ± 0.3 MPa for the three impact velocities; this is consistent with an absence of strain-rate (or inertial) hardening. However, after the initial peak in resistance, the measured and simulated flow stresses of the dynamically loaded samples gradually increased with strain, especially at the highest strain rate, and also exhibited several small additional stress peaks before the onset of densification (where the stress rose rapidly towards 25 MPa and beyond) at a strain $\varepsilon_D = 0.62 \pm 0.06$, which was less than the value of 0.72 measured under quasistatic deformation. These results are summarized in Table 4.

A sequence of high-speed video images and corresponding simulations for a notched tube impacted at $v_0 = 72 \, \text{ms}^{-1}$ are shown in Figure 6. The initial strain suffered by the impacted tube occurred by axial plastic compression of the tube walls at the notches. However, after a small shortening period as the tube walls at the notch compressed, the initial peak in strength was reached as the tube began to buckle about a notch, see Figure 6(a). This was initiated at the right-hand notch (nearest to impact end of the tube) at
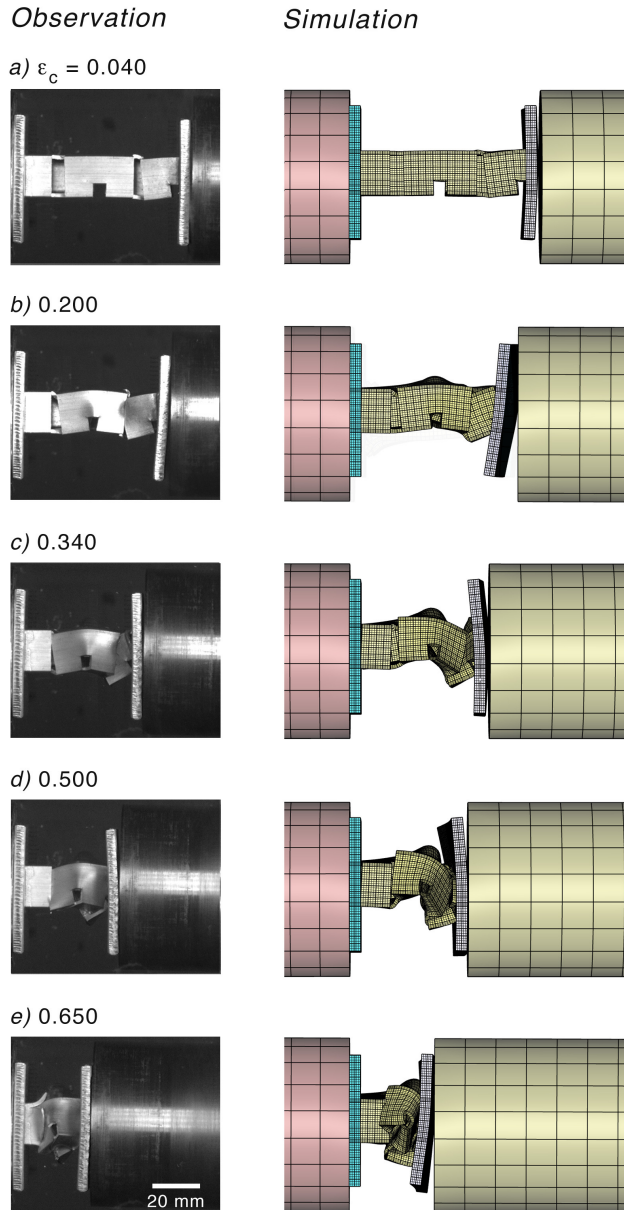
Figure 6. Observed and simulated deformation sequence for a (one-dimensional) notched tube specimen impacted at an initial velocity $v_0 = 72 \, \text{ms}^{-1}$. Impact occurs on the right side of both the photographs and the FE simulations.

a nominal strain of slightly less than 0.04, and correlated well with the first stress peak in Figure 5(b). As the nominal strain increased, new notch buckling events progressed from notches at the impact end of the sample towards those at the distal end, see Figure 6(a and b). At a nominal strain of 0.34, the tube walls near all the notches had suffered significant buckling deflections, see Figure 6(c), and material near the impact end had rotated about the notch. Further axial compression resulted in fracture of the buckled tube wall at the most distal notch, and contact of the tube walls on either side of this notch, as in Figure 6(d). This self-contact coincided with stiffening of the structure, and a rise in compressive flow stress to 4.7 MPa at a nominal strain of 0.56; see Figure 5(b). This process then progressed from right to left along the tube, resulting in densification at $\varepsilon_D = 0.65$; see Figure 5(b).

If the four notches had buckled (without tube rotation) until tube wall contact was established across the 6.35 mm-wide notch, the axial displacement of the 76.2 mm-long tube would have been 25.4 mm, a strain of 33%. Since the densification strain was about twice this value, we conclude that the combination of tube rotation and axial compression of the tube walls between the notches contributed about the same level of strain as notch deformation to the densification limit. We note that simulation images compared well to those observed with the high-speed camera (see Figure 6). The comparison was best when the strain was below 0.300. Beyond this strain, tube rotations were increasingly difficult to precisely predict due to the global nature of failure, and its sensitivity to imperfections. The simulations verified that the strength was governed by buckling collapse of the tubes, and that this was initiated at the right-hand notch nearest to the impact.

Increasing the impact velocity resulted in a similar deformation sequence, but the degree of tube rotation decreased with increased impact velocity (see Figure 7). This was observed in both the experimental data and in the simulation. Since tube rotation is an inertially sensitive failure mode, and was active during the nominal plateau region of the crush response, its decrease with increase in impact velocity may be responsible for the more rapid rise in plateau flow stress as the impact velocity increased; asee Figure 5(b–d). This would prolong axial tube compression (a harder mode) as opposed to tube rotation.

The total absorbed (plastically stored) energy per unit volume, E_v, was obtained from the area under the stress-strain curve shown in Figure 5(b). The integration was terminated at the densification strain, where the flow stress began to increase sharply due to material self-impingement. This gave a volumetric absorbed energy $E_v = 1.0$ MJ/m^3. Dividing this by the core density, $\bar{\rho}\rho_s = 0.067 \cdot 2.7$ Mg·m^{-3} = 180.9 kg·m^{-3}, gives a gravimetric absorbed energy, $E_m = 5.5$ J/g. If the stress achieved at the first stress peak had remained constant until densification, the gravimetric absorbed energy would have been the theoretical limit of the structure, $E_m^* = 9.2$ J/g. The notched one-dimensional structure impacted at $v_0 = 72$ m s^{-1} therefore had an energy absorption efficiency of 59.0%. The energy absorption and energy absorption efficiency of the tubes rose with impact velocity as the cores' peak strength also increased, see Table 4, and increased beyond unity (using the first stress peak to define the theoretical energy absorption) because of the gradual rise in plateau-region flow stress with strain in the most rapidly crushed samples. The FEA results slightly underpredicted the measured densification strains, most notably for the test at $v_0 = 157$ m s^{-1}.

The simulations permit calculation of the front-face pressure for each test, and this is overlaid on the experimental and predicted back-face responses of Figure 5. The initial inelastic impact resulted in very large contact stresses on the front-face sheet, and a significant momentum transfer to the lighter sandwich structure, leading to its loss of contact with the striker. As the tube-crushing reaction forces
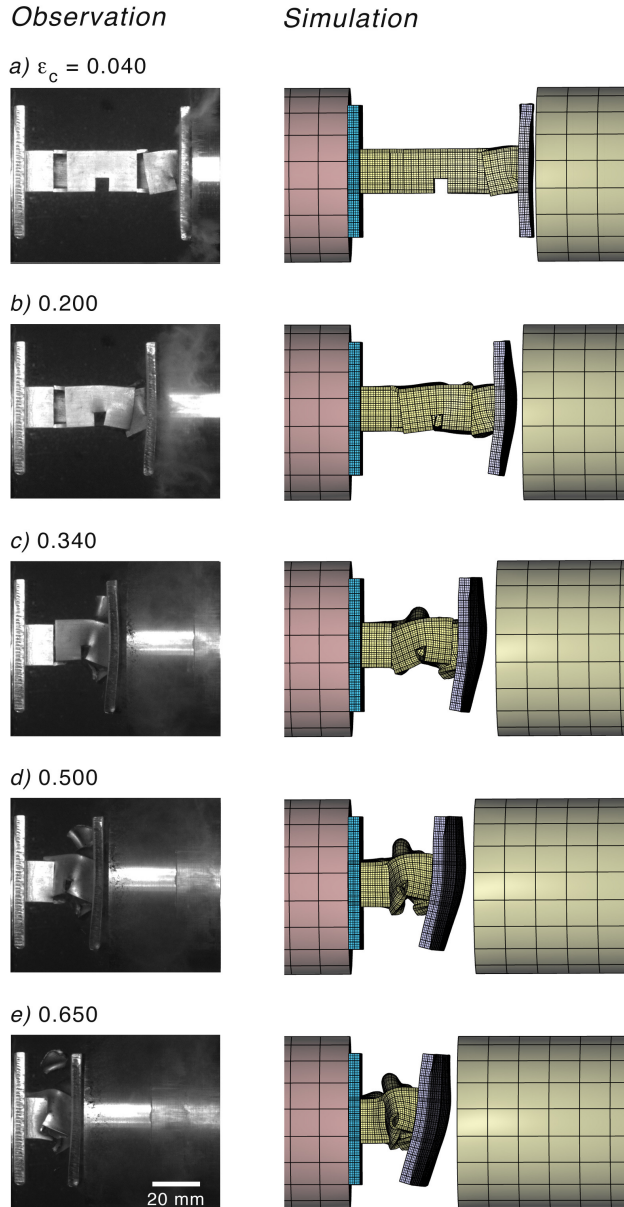
Figure 7. Experimentally observed and simulated deformation sequence for a notched (one-dimensional) tube specimen impacted at an initial velocity $v_0 = 157 \, \mathrm{m \, s^{-1}}$.

decelerated the impact face, the striker eventually recontacted the sample, and the stress once again increased. The repetition of this process is responsible for the series of stress peaks observed in the front-face stress-strain profiles, see Figure 5.

5.1.2. *Regular tube response.* The impact response of the vertical tube without notches is shown in Figure 8(b–d), and compared with that measured during quasistatic testing in Figure 8(a). The initial
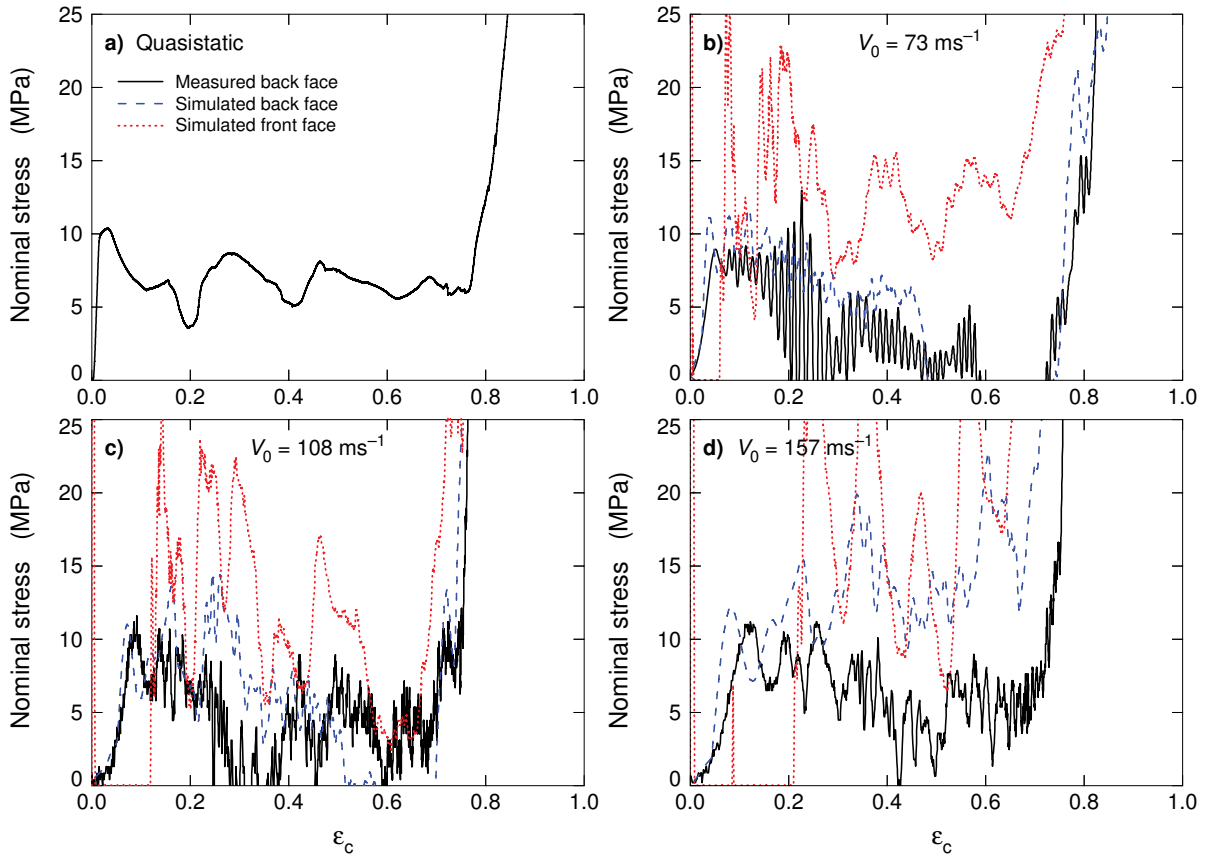
Figure 8. The measured and simulated back-face stress versus nominal compressive strain of an unnotched one-dimensional tube structure which contributed 7.3% to the relative density of the unnotched three-dimensional structure. (a) Quasistatic response, and for impacts at (b) $73\,\mathrm{ms}^{-1}$, (c) $108\,\mathrm{ms}^{-1}$, and (d) $157\,\mathrm{ms}^{-1}$. Simulation results are also shown for the front face of the specimen.

peak stress was again unaffected by the impact velocity, but had a much higher value of $\sim 11\,\mathrm{MPa}$ than that of a notched tube ($\sim 2.9\,\mathrm{MPa}$). The flow stress then dropped with continued loading, exhibiting numerous stress oscillations, until the onset of densification at a very high densification strain, $\varepsilon_D = 0.8$. The simulated back-face stress-strain responses are compared to experimental results in Figure 8, and are in reasonable agreement with the measurements considering the (small) experimental variability in the tube orientation. The measured peak strength and energy absorption for the samples are summarized in Table 4. Even though the initial peak strength was about four times that of the notched structure, and it had a higher densification strain, the volumetric energy absorption was only about twice that of the notched structure because of the substantial fall in strength following the initial peak in stress, and the highly oscillatory plateau region's response.

High-speed video and simulated images of the collapse process are shown in Figure 9. At low strains the tubes underwent plastic compression, and the initial peak in strength at $\varepsilon_c = 0.04\%$ was correlated with tube wall buckling; see Figure 9(a). This was followed by failure of the tube-front face bond, rotation of

the tube, and tube wall fracture at the apex of buckles; see Figure 9(b). This process continued resulting in fragmentation (and loss) of the tube walls. This delayed the onset of material self-impingement, and was the origin of the higher-than-normal densification strain; see Figure 9(e). The simulated damage progression in Figure 9 also shows the significant tube rotation and fragmentation of the tube during
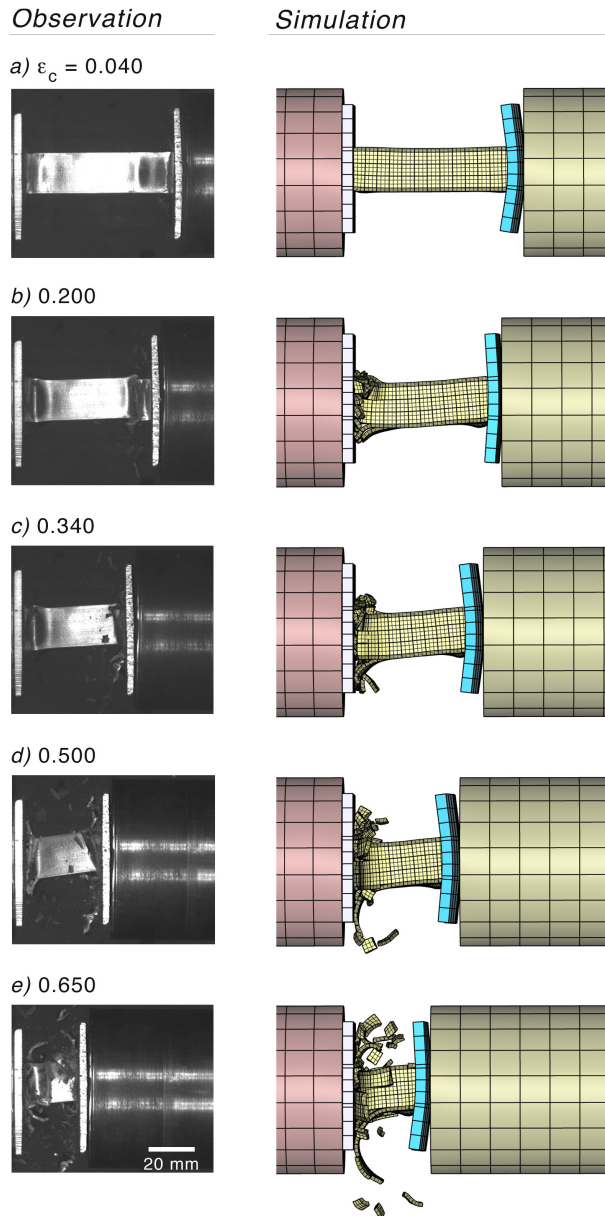
Figure 9. Observed and simulated deformation sequence for a one-dimensional tube specimen with a relative density of 7.3% and no notches impacted at an initial velocity $v_0 = 73 \, \text{ms}^{-1}$.

dynamic loading[2] observed experimentally. The "spiky" character of the measured stress profile was also seen in the simulation, and the transient partial load drops were linked to tube fracture events. The progressive drop in flow stress with continued straining arose from continued fragmentation at the distal end of the tube until densification at a strain of 0.8.

5.2. *Two-dimensional tube array.* The measured and simulated compressive stress versus strain response of the dynamically tested two-dimensional structure is shown in Figure 10(b–d) and compared to the quasistatic result in Figure 10(a). The stress versus strain responses at all loading rates exhibit three peaks followed by densification. The initial peak stress, σ_p was again independent of loading rate, which is consistent with minimal strain-rate hardening. The load dropped after each peak in stress resulted

---

[2]The response of the tube was highly sensitive to small changes in its orientation. When tubes were perfectly aligned, progressive concertina plastic buckling of the tubes was observed. However, introduction of the small misalignments present in the experiments resulted in the modes shown in the figures.
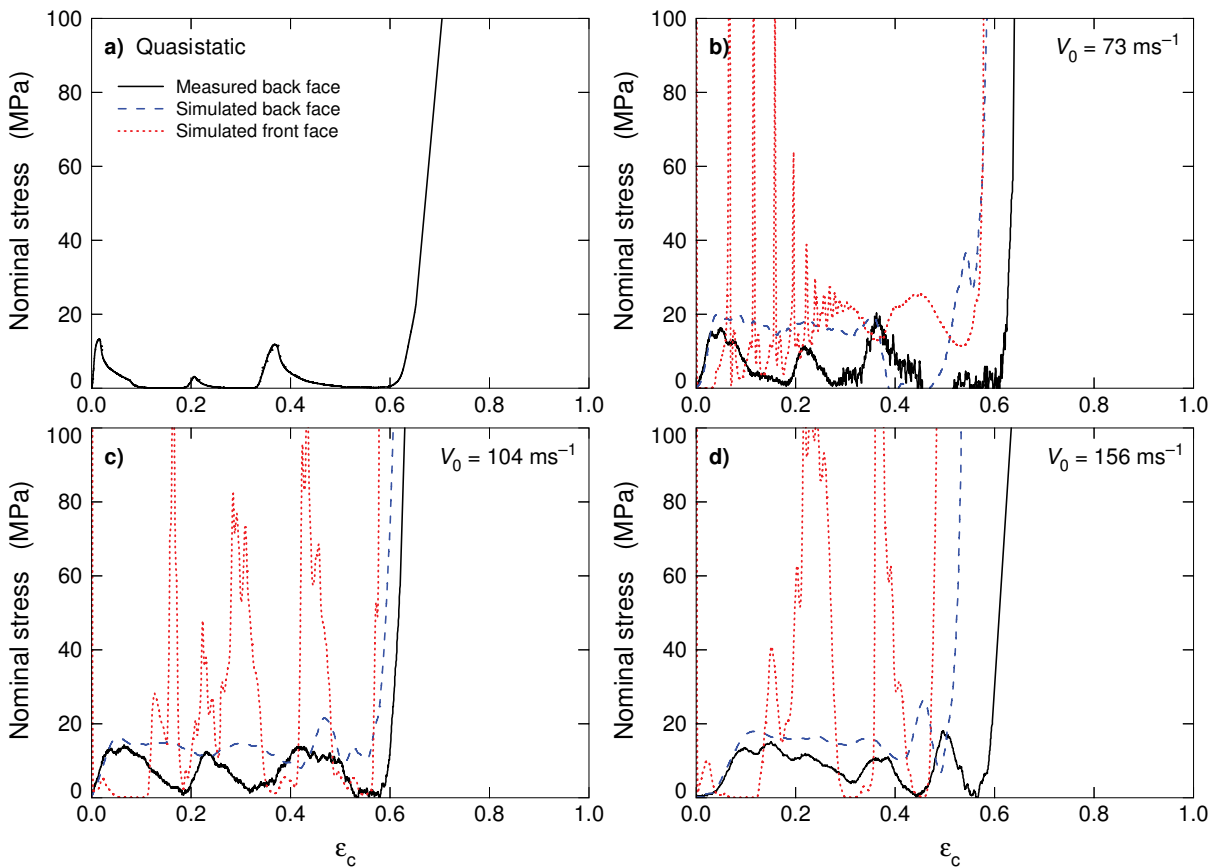
Figure 10. The measured and simulated dynamic stress versus normalized nominal strain responses of a two-dimensional tube structure with a relative density of 16.3%; (a) quasistatic response, and following impact at (b) $73\,\mathrm{ms}^{-1}$, (c) $104\,\mathrm{ms}^{-1}$, and (d) $156\,\mathrm{ms}^{-1}$.

in low volumetric and gravimetric energy absorptions (Table 4), but these (and the energy absorption efficiency) increased with impact velocity because the stress drops decreased in amplitude at higher velocities (Figure 10).

High-speed video observations and simulations (Figure 11) indicate that the initial rise to the first stress peak was always correlated with the onset of a high-order (short wavelength) buckling mode of
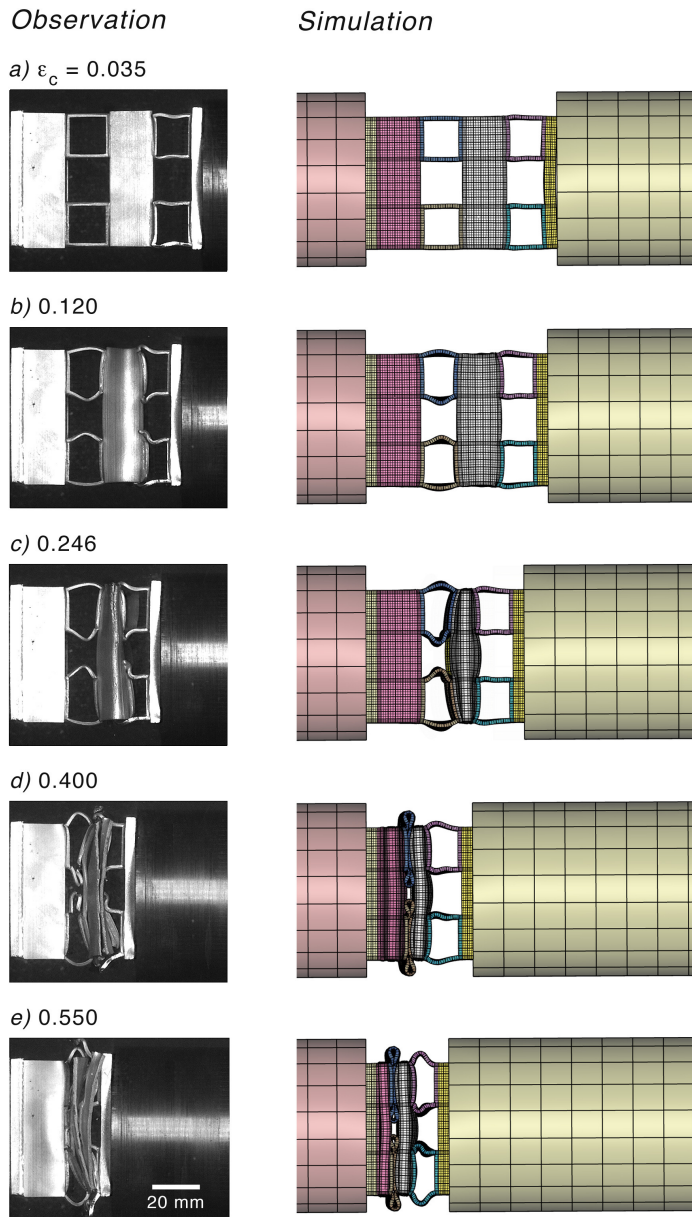
Figure 11. Observed and simulated deformation sequence for a two-dimensional specimen impacted at an initial velocity $v_0 = 73 \, \text{ms}^{-1}$.

the axially aligned walls of the tube layer nearest the impacted face; see Figure 11(a and b). As the sample continued to undergo compression, the buckling behavior became impact velocity dependent. At an impact velocity of $73 \, \text{ms}^{-1}$, buckling of the first-to-buckle (right-hand) layer stopped, as seen in Figure 11(b), and further strain was achieved by initiation of a low-order mode of buckling of the other three tube layers. As the compressive strain reached a value of about 0.2, the deformation localized into the tube layer second from the right in Figure 11(c), and the second peak in stress then corresponded to the collapse (aided by wall fracture) of this layer. The third stress peak corresponded to collapse of the tube layer third from the impacted end of the sample; see Figure 11(d). Collapse of the first impacted layer then coincided with the onset of densification at a strain of 0.62; see Figure 11(e). As the velocity of impact increased, the initial impact provided sufficient pressure to cause complete (but still high-order mode) buckling of the right-hand tube layer, and this collapse corresponded to the first peak in stress; see Figure 12(a and b). The other peaks then corresponded with the progressive collapse of the layers from right to left, as in Figure 12(c–e).

The simulated nominal stress versus applied nominal strain results shown in Figure 10(b–d) compared well with the experimental results. While the three peaks in stress are well predicted, the simulations do not fully capture the unloading instability, suggesting that the simulated tube wall fracture process is not completely captured by the approximate approach used here.

5.3. *Three-dimensional tube cores.*

5.3.1. *Notched vertical tube response.* The dynamic responses of the three-dimensional structures are shown in Figure 13(b–d) and are again compared to the quasistatic result in Figure 13(a). The three-dimensional cores' initial quasistatic peak strength, σ_p, was 20.9 MPa, while dynamically it was slightly less (varying from 17.2 to 18.2 MPa), and independent of impact velocity, see Table 4.[3]

In general, the dynamically deformed samples exhibited plateau-like compression responses with three small stress peaks like those associated with the sequential collapse of the two-dimensional in-plane tubes discussed above. The volumetric and gravimetric energy absorptions of the three-dimensional structures, seen in Table 4, were independent of compression rate. The average volumetric energy absorbed for the four loading rates was $9.2 \, \text{MJ/m}^3$. This significantly exceeded that for the average absorbed energy of $5.8 \, \text{MJ/m}^3$ for the components of the three-dimensional system (one notched tube and the two-dimensional tube array, see Table 5). The energy absorption efficiency of the three-dimensional structure was independent of the compression rate, and varied between 82 and 100%. The high efficiency resulted in part from the rising background stress just before densification was reached. This high efficiency, combined with the plateau-like compressive stress-strain response to compressive strains of about 50%, indicates the three-dimensional tube structure to be well suited for impact-mitigation applications.

The rear-face pressure responses from the finite element simulations were in good agreement with the measurements at the lowest impact velocity; see Figure 13(b). During quasistatic loading, three stress peaks were superimposed on a constant stress plateau response; see Figure 13(a). However, during dynamic loading, the third peak occurred on a rising background stress response and was most pronounced

---

[3]The difference in strength was consistent with small tube misalignments which have a significant effect upon the small samples tested here. To illustrate, Figure 14(a) shows a high-speed video image of the sample tested at $v_0 = 73 \, \text{ms}^{-1}$, and reveals that one of the in-plane tubes' side-walls (at the top right of the sample) was not in full contact with the underlying in-plane tube wall, causing it to prematurely fail.
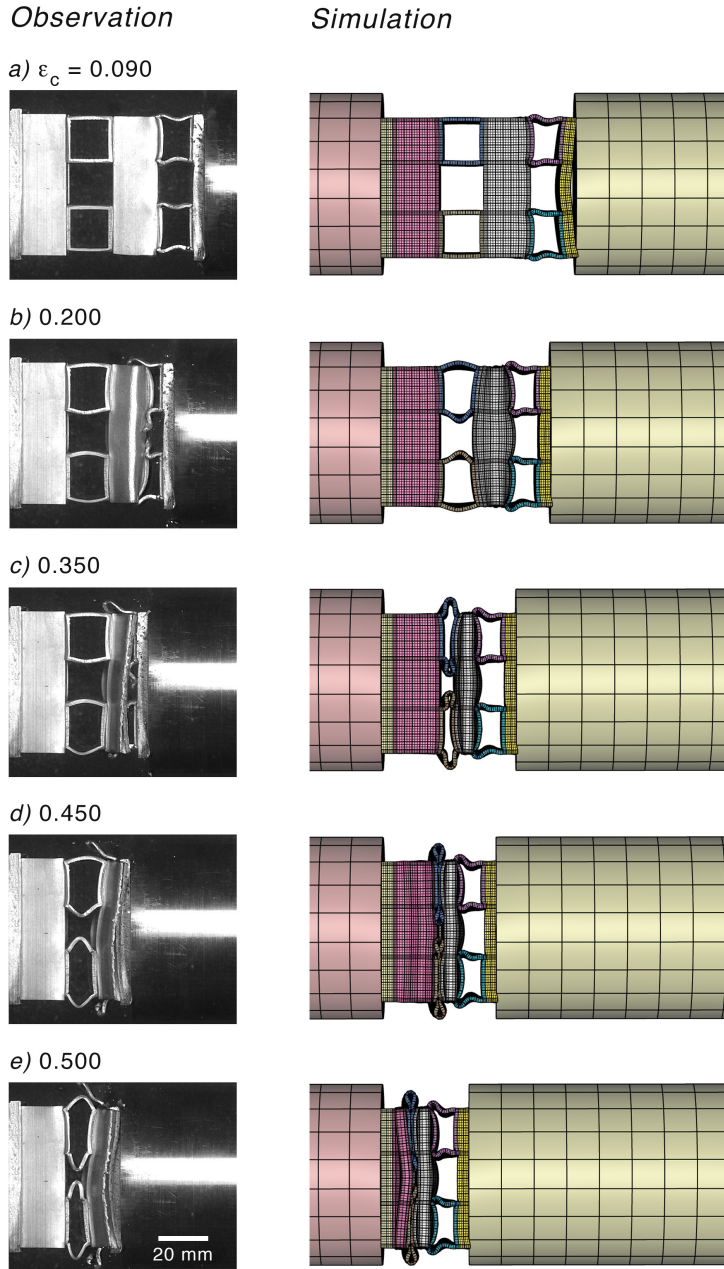
Figure 12. Observed and simulated deformation sequence for a two-dimensional specimen impacted at an initial velocity $v_0 = 156\,\text{ms}^{-1}$.

in the sample tested at the highest impact velocity; see Figure 13(d). This rising background stress was a characteristic of the vertical notched tube response; see Figure 5(c and d). A rise in predicted stress during the plateau response was also observed, but, for the two most rapidly loaded samples, exceeded that measured beyond a core strain of 20%. The small drops in flow stress after each peak were correlated
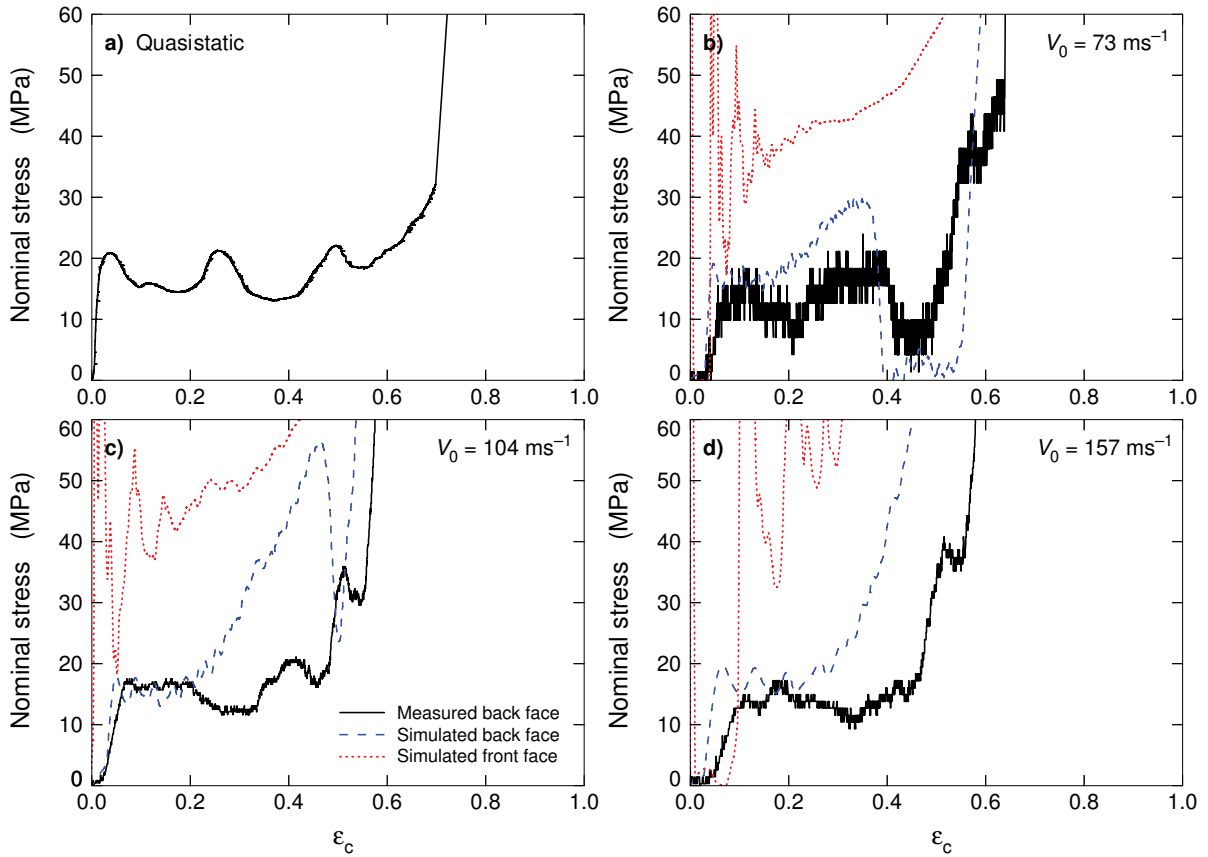
Figure 13. The measured and simulated dynamic stress versus nominal strain responses of a three-dimensional tube structure (containing notched out-of-plane tubes) with a relative density of 20.1%. (a) Quasistatic response, and after impact at (b) $73\,\mathrm{ms}^{-1}$, (c) $104\,\mathrm{ms}^{-1}$, and (d) $157\,\mathrm{ms}^{-1}$.

with the buckling instability and fracture of the walls of one of the collapsing tube layers of the four tube layer, $[0/90°]_2$ in-plane tube system.

The collapse mechanisms were investigated by examining a sequence of high-speed video images and finite element analyses. The result for an impact at $v_0 = 73\,\mathrm{ms}^{-1}$ is shown in Figure 14. The initial peak in stress occurred at a strain of 0.10; see Figure 13(b). From the experimental observations shown in Figure 14(b) this was correlated with both notch-induced out-of-plane tube collapse and the initiation of buckling of the in-plane tube walls, and was identical to the mechanism previously observed at quasistatic strain rates [Holloman et al. 2013]. By using the FEA postprocessor to make the in-plane tubes transparent after a simulation, as Figure 15(a), we see that by a core strain of 0.04, the notched tube had begun to buckle at the two notches nearest the impacted face. We were also able to confirm that notch-tripped buckling of the out-of-plane tube was coincident with in-plane buckling, a result consistent with the earlier observations that the components (single-axial and two-dimensional tube arrays) of the three-dimensional cellular structure also buckled at the same strain (4%).
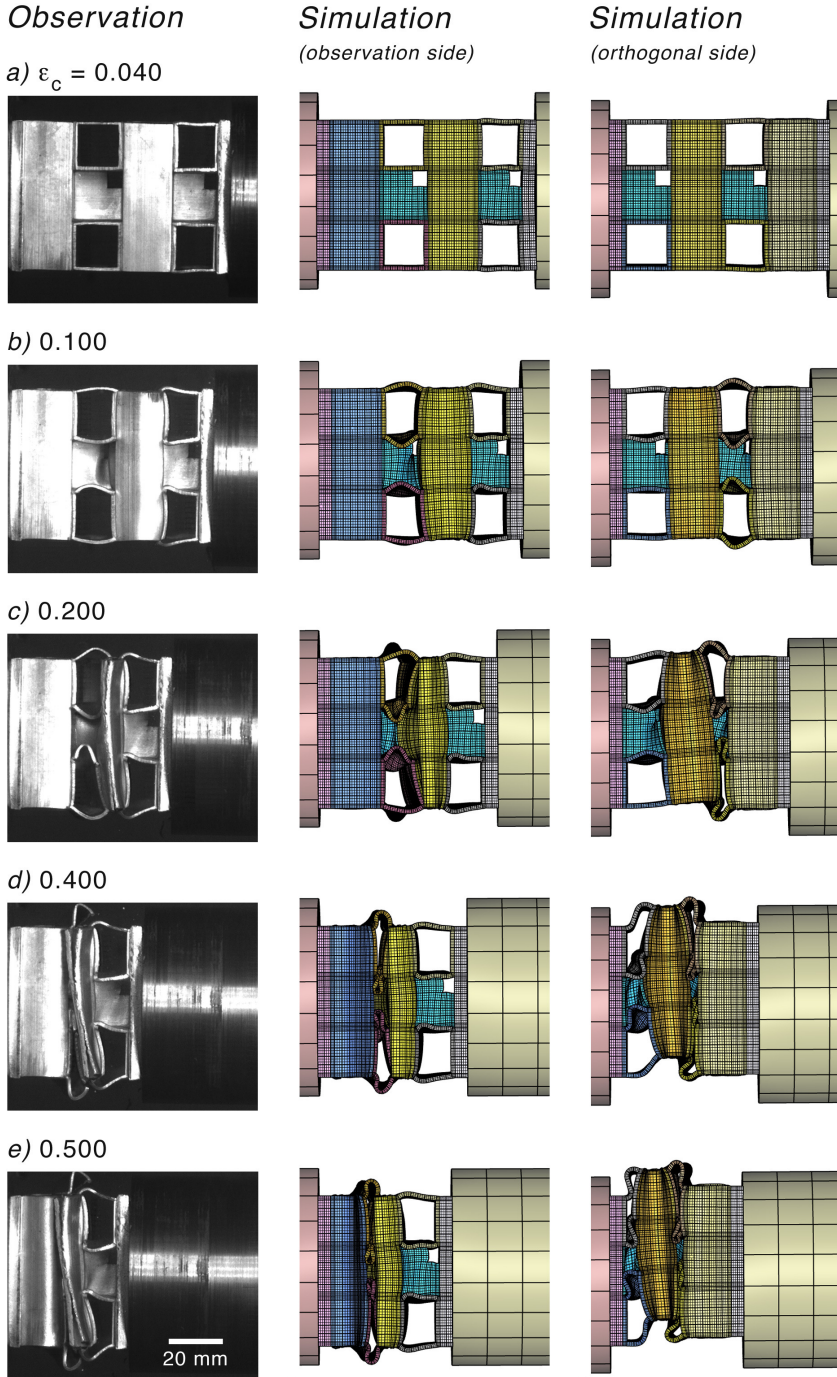
Figure 14. Observed and simulated deformation sequence for a three-dimensional specimen with a relative density of 20.1% after impact at an initial velocity $v_0 = 73\,\text{ms}^{-1}$. Two sides of the simulated FE model are shown to more clearly reveal the deformation sequence.
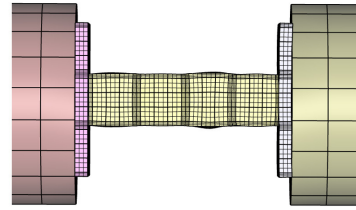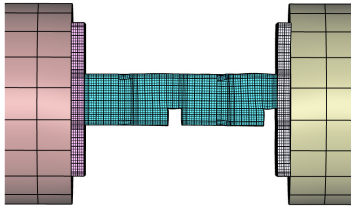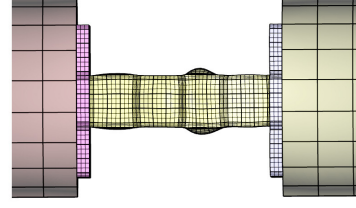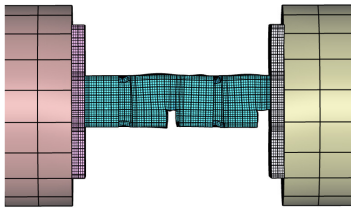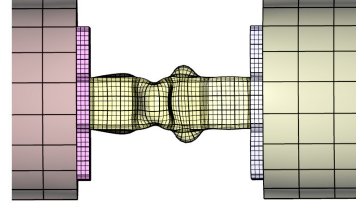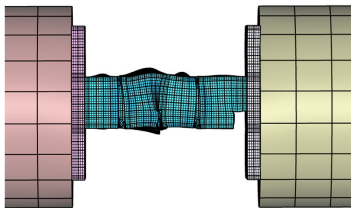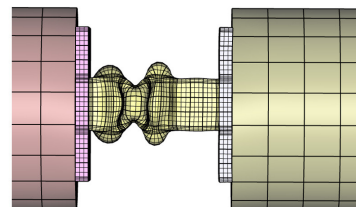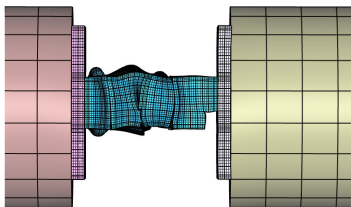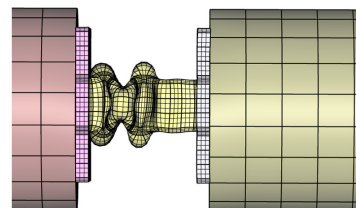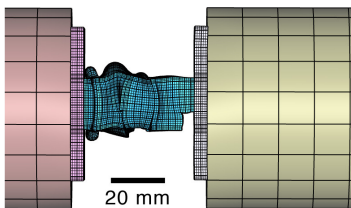
**Figure 15.** Deformation sequence showing the three-dimensional notched and un-notched structures when the colinear tubes have been made transparent to show the collapse mode of the axial aligned tubes following impact at an initial velocity $v_0 = 73 \, \text{ms}^{-1}$.

Topology	$\sum \bar{\rho}$	v (ms^{-1})	$\sum \sigma_p$ (MPa)	E_v (MJ/m^3)	E_m (J/g)
Notched 1D tube with 2D core	23.0	0	17.9	2.8	5.2
		72	17.4	4.4	8.2
		105	17.3	7.2	13.3
		157	16.8	8.9	16.4
Unnotched 1D tube with 2D core	23.6	0	23.2	6.1	9.5
		73	25.1	4.8	8.5
		108	25.6	8.7	15.4
		157	25.6	11.5	20.3

Table 5. Summed responses of one and two-dimensional cores (including the sum of the relative densities, $\bar{\rho}$, the impact velocity, v, and the sum of the compressive strengths, σ_p). (The sums of the one and two-dimensional cores do not match the measured relative density of the three-dimensional core because of variability in tube wall thickness resulting from the extrusion process and an effect of the braze layer.)

Further compression beyond the initial stress peak resulted in the flow stress softening to a strain of $\sim 20\%$. The high-speed video images and the simulations, shown in Figure 14(c), indicate this corresponded with continued buckling of the second in-plane tube layer from the strike face, consistent with observations of the two-dimensional in-plane structure at this impact rate; see Figure 11(a). Collapse of the second layer, rather than that nearest the strike face, appears to have resulted from its higher-order buckling mode, which requires a higher stress to continue collapse. Following this softening, the tested structure hardened to a second stress peak at a strain of 0.38 followed by a sharp drop in stress at a strain of 0.41. The mechanism responsible for the structures' rapid stress drop can be seen by comparing the high-speed images and simulations in Figure 14(c and d). It resulted from the buckling collapse of the third layer of tubes from the strike face. The orthogonal simulated view of the collapse process in Figure 14 also reveals a significant lateral (transverse shear) displacement as the axial strain increased to 0.4. The simulations also revealed that the second and fourth notches from the impact face contributed to the shearing of the second and fourth in-plane tube layers. This mechanism is not apparent in the high-speed video images due to the orientation of the specimen. Further collapse of the structure resulted in core densification (with additional shear of the second and fourth in-plane tube layers) as the fourth in-plane layer and the first in-plane tube layer buckled at $\varepsilon_D = 0.61$.

It is interesting to note that as the impact velocity increased, the transverse (shear) displacement was reduced, and at the highest impact velocity the structure collapsed axially with no transverse displacement; this was observed by both experiment and simulation (Figure 16). This change in deformation mode appears to be linked with the collapse of the vertical notched tube which during isolated testing (see Figures 6 and 7), exhibited significant rotation and transverse displacement at low velocities, but deformed in a more axial manner at the highest impact velocity. To investigate this we show the simulated deformation sequence of the axial tubes of the three-dimensional sample tests conducted at 73 and 157 ms^{-1} in Figure 17. It can be seen that a significant lateral deformation accompanies the low-velocity test, but at high velocities, the sample progressively collapsed with no transverse motion.
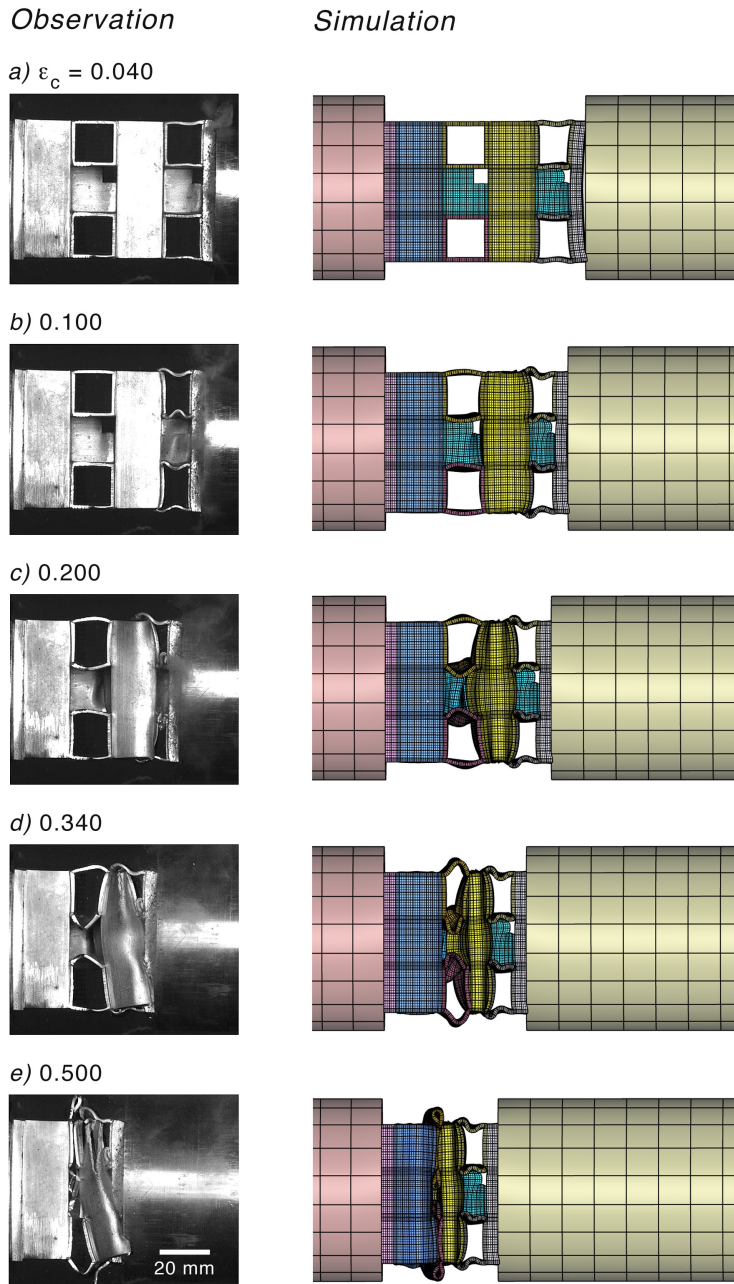
Figure 16. Observed and simulated deformation sequence for a three-dimensional specimen with a relative density of 20.1% after impact at an initial velocity $v_0 = 157\,\text{ms}^{-1}$.

The simulations indicate the initial contact stresses between the projectile and the front-face sheet increased from 764 to 1520 MPa as the impact velocity increased from 73 to 157 ms^{-1}, and greatly exceed those at the distal end of the samples; see Figure 13(b–d). Following striker impact at $v_0 = 73\,\text{ms}^{-1}$,
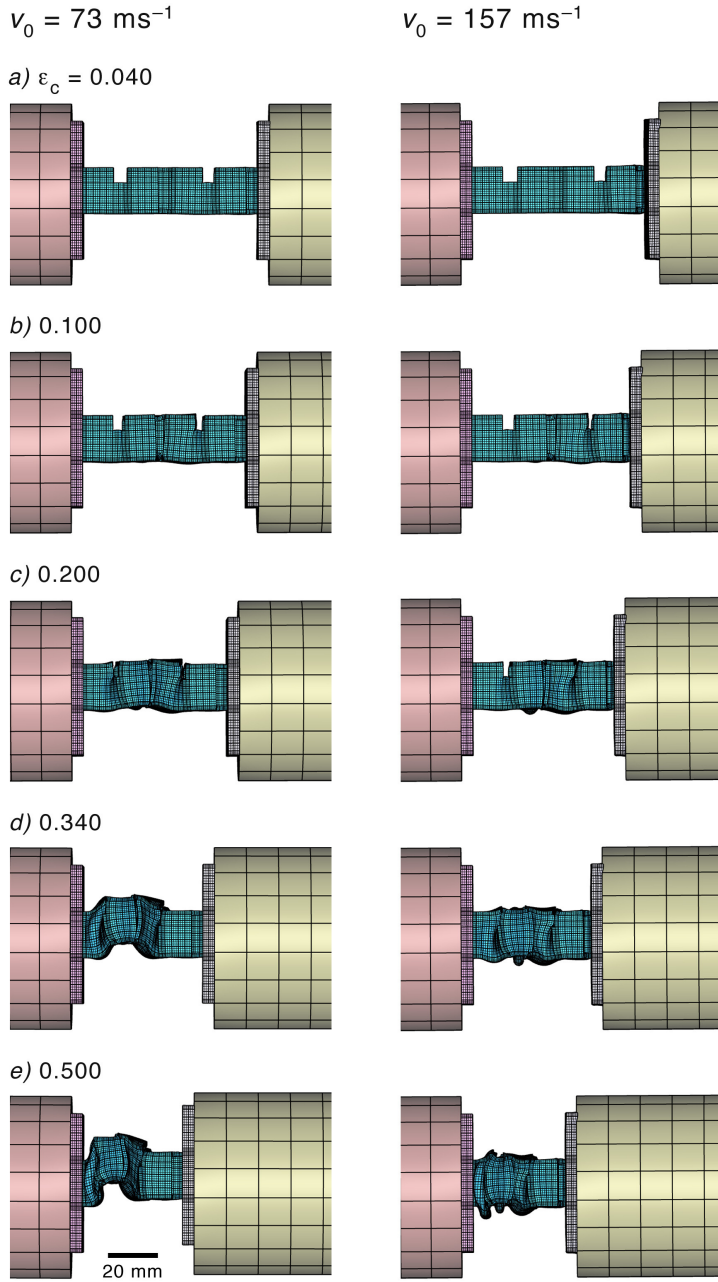
Figure 17. Deformation sequence showing the orthogonal side of the three-dimensional notched structure after the colinear tubes have been made transparent.

the three-dimensional sample was brought into equilibrium much more quickly than the one or two-dimensional cores, because of its higher mass and core strength. However, as the initial impact velocity was increased, larger amounts of energy were transferred to the specimen during initial contact, and the

contact force briefly dropped to zero for impact at $v_0 = 157\,\mathrm{m\,s}^{-1}$ as sample face sheet-striker separation occurred; see Figure 13(d).

Three-dimensional tube cores with relative densities $\bar{\rho} = 11.6$ and 42.7% were also tested; the results are summarized in Table 4. The structure with $\bar{\rho} = 11.6\%$ was observed to fail in a similar fashion as the $\bar{\rho} = 20.1\%$ structure. At the lowest impact velocity transverse (shear) displacement was present, but at the highest impact velocity the structure collapsed axially with no transverse shear, which resulted in increased flow stress. The three-dimensional cores with a relative density of 42.7% were not completely crushed during dynamic loading, even though the striker was reflected from the specimen (thereby increasing the transferred momentum and applied pressure). While the initial strength could be measured (and is given in Table 4), it was not possible to determine the densification strain or energy absorbed by this structure. Simulations indicated that the out-of-plane notched tube in the highest density structure showed no rotation, ever at the lowest impact velocity, where rotation was observed in the other two structures.

5.3.2. *Regular vertical tube three-dimensional case.* The three-dimensional core without notches in the vertical tubes ($\bar{\rho} = 21.0\%$)[4] was tested dynamically to determine the role of the notches upon the response of the three-dimensional structure. The measured and simulated compressive stress-strain responses for impacts at various velocities are shown in Figure 18. The samples tested at impact velocities of 73 and $108\,\mathrm{m\,s}^{-1}$ exhibited several small peaks in stress during the region of plateau response like those seen in the two and three-dimensional structure with notched axial tubes. These stress peaks corresponded to the sequential collapse of three of the in-plane tube layers; see Figure 19. Collapse of the fourth layer coincided with densification (in simulations, the first layer was responsible for densification). The sample tested at the highest impact velocity, as shown in Figure 18(d), exhibited almost no secondary peaks and had an almost ideal plateau response to a densification strain of about 0.6 (about the same as the quasistatic test).

The mechanical properties of the cores are summarized in Table 4. The cores were slightly stronger than their notched counterparts, consistent with the higher strength of the unnotched out-of-plane tube. The first peak stress and densification strains were again independent of impact velocity. The average volumetric energy absorbed was $10.9\,\mathrm{MJ/m^3}$, compared to $7.8\,\mathrm{MJ/m^3}$ for the average of the summed component tubes (see Table 5) indicating much less of a synergistic energy absorption effect in this three-dimensional structure. The energy absorption efficiencies range between 62 and 82% (see Table 4) for these cores, making them quite efficient.

Recall that in Section 5.1 a regular tube not in perfect axial alignment with the striker underwent tube rotation and buckling with fragmentation. Stress drops were observed to accompany the fracture events. Comparison of the single tube (Figure 8) and three-dimensional (Figure 18) responses reveals significantly reduced load drops suggesting that vertical tube fragmentation was suppressed. Using the FEA postprocessor to make in-plane tubes transparent, the out-of-plane (unnotched) tube walls are shown to have concertina buckled in Figure 15 as opposed to rotation, buckling, and fragmentation fracture (Figure 9). This appears to be the origin of the extra energy absorbed in the three-dimensional structures compared to their one-dimensional and $[0°/90°]_2$ tube components.

---

[4]Its density was less than the sum of the one-dimensional tube and two-dimensional structure due to variations of $\pm 0.14\,\mathrm{mm}$ in the thickness of the tube walls.
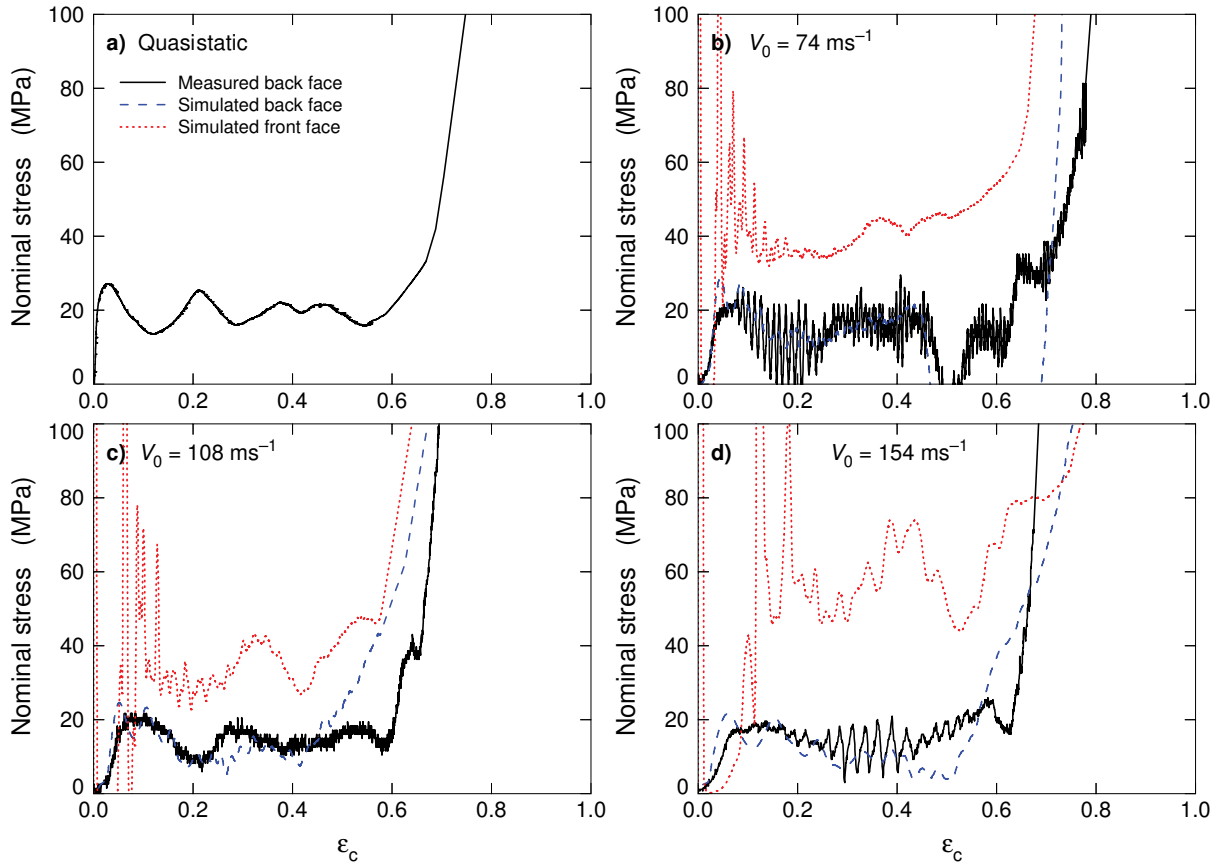
Figure 18. The measured and simulated dynamic stress versus normalized nominal strain responses of a three-dimensional tube structure that used out-of-plane tubes without notches. Its relative density was 21.0%. (a) Quasistatic response, and following impact at (b) $74\,\mathrm{m\,s^{-1}}$, (c) $108\,\mathrm{m\,s^{-1}}$, and (d) $154\,\mathrm{m\,s^{-1}}$.

6. Discussion

Figure 20(a) summarizes dependence of the initial compressive peak stress, σ_p, for the three-dimensional notched structures and their components as a function of the impact velocity, v_0, and applied strain rate, $\dot{\varepsilon}_c = v_0/h$ (upper scale). The results confirm that the structures' initial compressive strength is insensitive to the rate of loading for strain rates up to $2000\,\mathrm{s^{-1}}$. Detailed observations indicate that the axial compression of single notched tubes proceeds by plastic compression of the tube walls followed by buckling at the notches and then of the tube segments between the notches; see Figures 6 and 7. The rotation of the tubes became increasingly relevant after crushing to strains of 20%, and was reduced by increasing the rate of compression, consistent with a [Calladine and English 1984] Type II structure. The suppression of the Type II behavior in rapidly compressed samples was linked with a rise in flow stress with plastic strain during plateau-region compression of single tubes and the three-dimensional structures that contained them (see Figure 13).
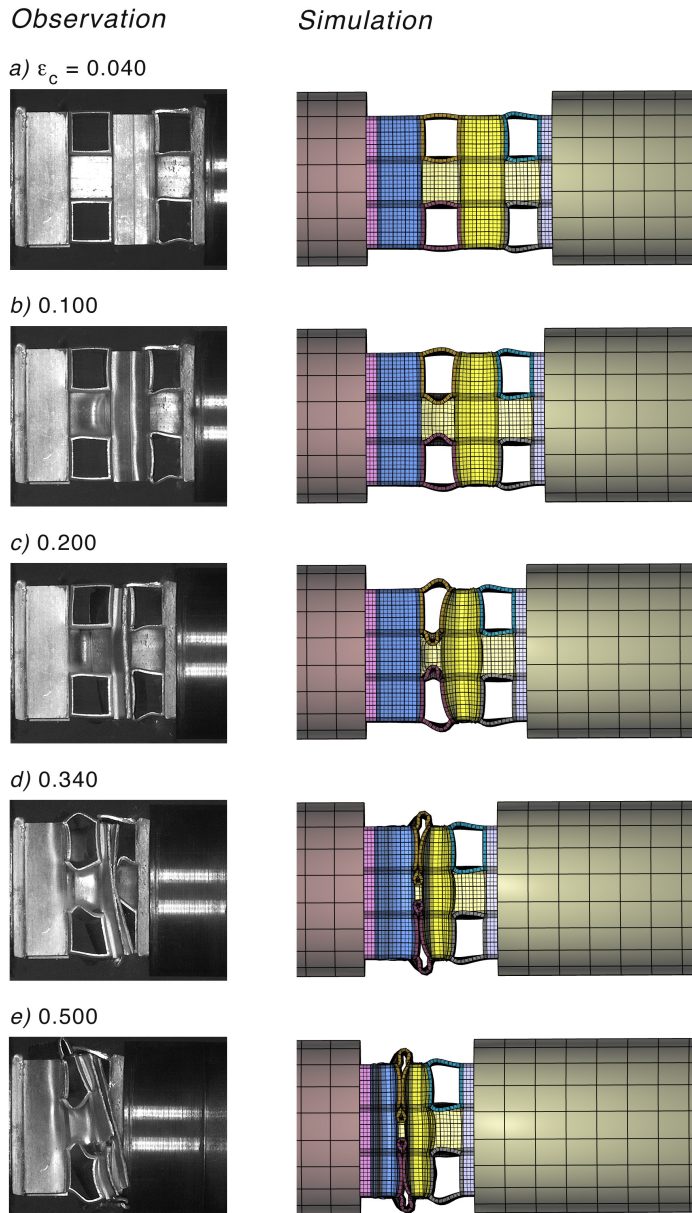
Figure 19. Observed and simulated deformation sequence for a three-dimensional specimen whose four vertical tubes had no notches in the axial aligned tube. The sample relative density was 21.0%, and it was impacted at an initial velocity $v_0 = 74\,\mathrm{m\,s^{-1}}$.

The [0/90°]$_2$ in-plane tube structures failed by plastic buckling of the tubes walls aligned with the crush direction, and was accompanied by three significant load drops. At low impact velocities, lateral displacement of the tubes (transverse to the loading direction) also occurred. As this lateral displacement was suppressed at higher impact velocities, the drop in load was reduced and the average stress prior to densification increased; see Figure 10.
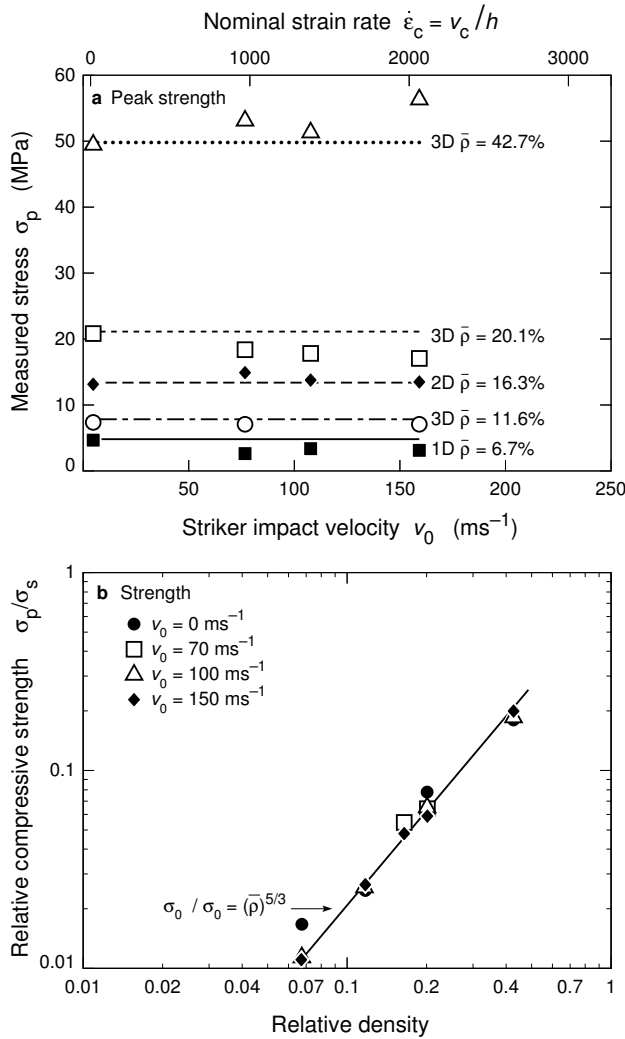
Figure 20. (a) Measured back-face stresses for the notched tube core structures as a function of impact velocity on applied strain rate for the initial stress profile peak. The horizontal dashed lines correspond to an extension of the quasistatic strength. (b) Dependence of compressive strength upon relative density with an empirical fit.

The combination of the notched vertical tubes and $[0/90°]_2$ lay-up to form the three-dimensional structure resulted in an increase in plastic energy absorption that significantly exceeded the sum of the energy absorptions of the individual vertical tubes and two-dimensional lay-up; see Table 5. Analysis of the finite element simulations has revealed that it was a result of suppression of the vertical notched tubes' rotation by the in-plane tubes. The axial strain was then achieved by a greater contribution from plastic compression of the tubes' walls — a more energy-absorbing mechanism than rotation.

Removal of the notches from the vertical tubes increased the axial compressive strength of the tubes. Their mode of compression when made from an alloy in its peak aged state was highly dependent upon the orientation of tubes. The small misalignments present in experiments resulted in a low-order buckling

mode during initial deformation, followed by rotation and progressive fragmentation. Numerous load drops associated with the fragmentation were observed, and the rotation resulted in a general reduction in compression resistance. Inserting the unnotched tubes in the three-dimensional structure increased the strength of the structure over that of a similar-density three-dimensional structure containing notched tubes, and led to a synergistic effect upon the energy absorption. In this case, detailed analysis of the finite element simulations revealed that the in-plane tubes suppressed rotation and forced the vertical tubes to concertina buckle with additional energy absorption.

Figure 20(b) shows that the variation in peak strength, σ_p, of the notched three-dimensional structures with relative densities between 11 and 43% scaled by the strength of the alloy, σ_s, from which they are made. The strength exhibits a power dependence upon relative density:

$$\sigma_p/\sigma_s = (\bar{\rho})^{5/3}. \tag{4}$$

This agrees with both the experimental data and FE predictions for the structures tested quasistatically [Holloman et al. 2013]. The dynamically tested structures at all tested impact velocities scale with relative density to the power 5/3, and like the quasistatic results, this suggests the response is dominated by the out-of-plane tubes. By tailoring the in and out-of plane tube walls the three-dimensional structure can be made anisotropic and the compressive strengths will be based on the power law, (4), as shown quasistatically in [Holloman et al. 2013].

The simulation procedure used here has successfully modeled both the rear-face pressure versus compression strain response and the mechanisms of core collapse. It was therefore used to estimate the front (impact) face contact pressure which was not measured in these experiments. During an impact, the contact pressure and frontal displacement determine the work done by the impact mitigators. The simulations indicate that the ratio of the front to rear-face pressure is linearly related to the impact velocity and inversely dependent upon the relative density of the cellular structure; see Figure 21. However, the front-face pressure is much higher than that at the rear of the specimens and increases with both core density and impact velocity, suggesting that this structure may be well suited for mitigating high-intensity dynamic loads.
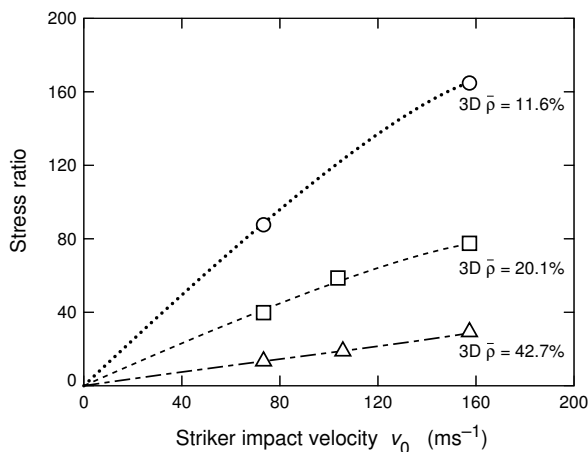

Figure 21. Simulated stress ratio based on the initial peak stress calculated for the front and back faces of the sandwich structures with notched cores.

7. Conclusion

We have fabricated aluminum 6061-T6 sandwich-panel structures with cores made from a two-dimensional $[0°/90°]_2$ arrangement of tubes with either notched or unnotched orthogonal tubes inserted in the out-of-plane direction. The resulting three-dimensional tube cores had relative densities between 11 and 43%. A combination of instrumented Kolsky bar impact experiments, high-speed video imaging, and finite element simulations using a rate-dependent, piecewise-linear hardening model with a von Mises multiaxial yield surface and a simplified failure criterion were used to investigate the dynamic compressive response of the three-dimensional tube core sandwich structure and the two-dimensional and out-of-plane-tubes from which they were constructed. We have found that:

(1) A three-dimensional tube structure of a given relative density has a near-constant crush strength to a strain of about 60%. The initial compressive strength is independent of impact velocity for compression strain rates up to $2000 \, \text{s}^{-1}$, which was verified with the simulated model to be a consequence of the rate-independent plastic response of the aluminum 6061-T6 alloy.

(2) The core strength exhibited a power-law dependence upon relative density, given by $\sigma_p/\sigma_s = (\bar{\rho})^{5/3}$, consistent with crush strengths controlled by the buckling of tubes oriented in the applied-load direction.

(3) The vertical tube response of the tubes was rate-dependent due to tube rotation at low impact velocities.

(4) The vertical tube collapse mode changes when placed inside the in-plane tube lay-up, leading to a synergistic interaction in the energy absorption between the colinear aligned and vertical tubes at dynamic loading, which was also observed with quasistatic loading.

(5) The finite element simulations reveal that the ratio of the impact to back-face stresses increased with strain rate and core density, which is a valuable result for shock load mitigation problems.

8. Acknowledgements

References

[Abramowicz and Jones 1997] W. Abramowicz and N. Jones, "Transition from initial global bending to progressive buckling of tubes loaded statically and dynamically", *Int. J. Impact Eng.* **19**:5–6 (1997), 415–437.

[Allen 1969] H. G. Allen, *Analysis and design of structural sandwich panels*, Pergamon, Oxford, 1969.

[Baumeister et al. 1997] J. Baumeister, J. Banhart, and M. Weber, "Aluminium foams for transport industry", *Mater. Des.* **18**:4–6 (1997), 217–220.

[Bitzer 1997] T. Bitzer, *Honeycomb technology: materials, design, manufacturing, applications and testing*, 1st ed., Chapman & Hall, London, 1997.

[Calladine and English 1984] C. R. Calladine and R. W. English, "Strain-rate and inertia effects in the collapse of two types of energy-absorbing structure", *Int. J. Mech. Sci.* **26**:11–12 (1984), 689–701.

[Cockcroft and Latham 1968] M. G. Cockcroft and D. J. Latham, "Ductility and workability of metals", *J. Inst. Met.* **96**:1 (1968), 33–39.

[Dannemann and Lankford 2000] K. A. Dannemann and J. Lankford, Jr., "High strain rate compression of closed-cell aluminium foams", *Mater. Sci. Eng. A* **293**:1–2 (2000), 157–164.

[Deshpande and Fleck 2000] V. S. Deshpande and N. A. Fleck, "High strain rate compressive behaviour of aluminium alloy foams", *Int. J. Impact Eng.* **24**:3 (2000), 277–298.

[Deshpande and Fleck 2005] V. S. Deshpande and N. A. Fleck, "One-dimensional response of sandwich plates to underwater shock loading", *J. Mech. Phys. Solids* **53**:11 (2005), 2347–2383.

[Dharmasena et al. 2009] K. P. Dharmasena, D. T. Queheillalt, H. N. G. Wadley, Y. C. Chen, P. Dudt, D. Knight, Z. Wei, and A. G. Evans, "Dynamic response of a multilayer prismatic structure to impulsive loads incident from water", *Int. J. Impact Eng.* **36**:4 (2009), 632–643.

[Dharmasena et al. 2011] K. P. Dharmasena, H. N. G. Wadley, K. Williams, Z. Xue, and J. W. Hutchinson, "Response of metallic pyramidal lattice core sandwich panels to high intensity impulsive loading in air", *Int. J. Impact Eng.* **38**:5 (2011), 275–289.

[Dharmasena et al. 2013] K. P. Dharmasena, H. N. G. Wadley, T. Liu, and V. S. Deshpande, "The dynamic response of edge clamped plates loaded by spherically expanding sand shells", *Int. J. Impact Eng.* **62** (2013), 182–195.

[Elzey and Wadley 2001] D. M. Elzey and H. N. G. Wadley, "The limits of solid state foaming", *Acta Mater.* **49**:5 (2001), 849–859.

[Evans et al. 2001] A. G. Evans, J. W. Hutchinson, N. A. Fleck, M. F. Ashby, and H. N. G. Wadley, "The topological design of multifunctional cellular metals", *Prog. Mater. Sci.* **46**:3–4 (2001), 309–327.

[Ferri et al. 2006] E. Ferri, E. Antinucci, M. Y. He, J. W. Hutchinson, F. W. Zok, and A. G. Evans, "Dynamic buckling of impulsively loaded prismatic cores", *J. Mech. Mater. Struct.* **1**:8 (2006), 1345–1365.

[Fyllingen et al. 2010] Ø. Fyllingen, O. S. Hopperstad, A. G. Hanssen, and M. Langseth, "Modelling of tubes subjected to axial crushing", *Thin-Walled Struct.* **48**:2 (2010), 134–142.

[Hanssen and Olovsson 2013] A. G. Hanssen and L. Olovsson, "IMPETUS Afea Solver", 2013, http://www.impetus-afea.com/solver.

[Hanssen et al. 2000a] A. G. Hanssen, O. S. Hopperstad, and M. Langseth, "Static and dynamic crushing of square aluminium extrusions with aluminium foam filler", *Int. J. Impact Eng.* **24**:4 (2000), 347–383.

[Hanssen et al. 2000b] A. G. Hanssen, L. Lorenzi, K. K. Berger, O. S. Hopperstad, and M. Langseth, "A demonstrator bumper system based on aluminium foam filled crash boxes", *Int. J. Crashworthiness* **5**:4 (2000), 381–392.

[Hanssen et al. 2001] A. G. Hanssen, O. S. Hopperstad, and M. Langseth, "Design of aluminium foam-filled crash boxes of square and circular cross-sections", *Int. J. Crashworthiness* **6**:2 (2001), 177–188.

[Holloman et al. 2013] R. L. Holloman, V. S. Deshpande, A. G. Hanssen, K. M. Fleming, J. R. Scully, and H. N. G. Wadley, "Tubular aluminum cellular structures: fabrication and mechanical response", *J. Mech. Mater. Struct.* **8**:1 (2013), 65–94.

[Johnson 1972] W. Johnson, *Impact strength of materials*, Edward Arnold, London, 1972.

[Kolsky 1949] H. Kolsky, "An investigation of the mechanical properties of materials at very high rates of loading", *Proc. Phys. Soc. B* **62**:11 (1949), 676–700.

[Kooistra et al. 2004] G. W. Kooistra, V. S. Deshpande, and H. N. G. Wadley, "Compressive behavior of age hardenable tetrahedral lattice truss structures made from aluminium", *Acta Mater.* **52**:14 (2004), 4229–4237.

[Kooistra et al. 2008] G. W. Kooistra, D. T. Queheillalt, and H. N. G. Wadley, "Shear behavior of aluminum lattice truss sandwich panel structures", *Mater. Sci. Eng. A* **472**:1–2 (2008), 242–250.

[Maiti et al. 1984] S. K. Maiti, L. J. Gibson, and M. F. Ashby, "Deformation and energy absorption diagrams for cellular solids", *Acta Metall.* **32**:11 (1984), 1963–1975.

[Moongkhamklang and Wadley 2010] P. Moongkhamklang and H. N. G. Wadley, "Titanium alloy lattice structures with millimeter scale cell sizes", *Adv. Eng. Mater.* **12**:11 (2010), 1111–1116.

[Pingle et al. 2011] S. M. Pingle, N. A. Fleck, V. S. Deshpande, and H. N. G. Wadley, "Collapse mechanism maps for a hollow pyramidal lattice", *Proc. R. Soc. Lond. A* **467**:2128 (2011), 985–1011.

[Queheillalt et al. 2000] D. T. Queheillalt, H. N. G. Wadley, B. W. Choi, and D. S. Schwartz, "Creep expansion of porous Ti-6Al-4V sandwich structures", *Metall. Mater. Trans. A* **31**:1 (2000), 261–273.

[Queheillalt et al. 2008] D. T. Queheillalt, Y. Murty, and H. N. G. Wadley, "Mechanical properties of an extruded pyramidal lattice truss sandwich structure", *Scr. Mater.* **58**:1 (2008), 76–79.

[Radford et al. 2007] D. D. Radford, G. J. McShane, V. S. Deshpande, and N. A. Fleck, "Dynamic compressive response of stainless-steel square honeycombs", *J. Appl. Mech.* (*ASME*) **74**:4 (2007), 658–667.

[Reid 1993] S. R. Reid, "Plastic deformation mechanisms in axially compressed metal tubes used as impact energy absorbers", *Int. J. Mech. Sci.* **35**:12 (1993), 1035–1052.

[Reyes 2008] G. Reyes, "Static and low velocity impact behavior of composite sandwich panels with an aluminum foam core", *J. Compos. Mater.* **42**:16 (2008), 1659–1670.

[Rimoli et al. 2011] J. J. Rimoli, B. Talamini, J. J. Wetzel, K. P. Dharmasena, R. Radovitzky, and H. N. G. Wadley, "Wet-sand impulse loading of metallic plates and corrugated core sandwich panels", *Int. J. Impact Eng.* **38**:10 (2011), 837–848.

[Russell et al. 2010] B. P. Russell, A. Malcom, H. N. G. Wadley, and V. S. Deshpande, "Dynamic compressive response of composite corrugated cores", *J. Mech. Mater. Struct.* **5**:3 (2010), 477–493.

[Shahdin et al. 2009] A. Shahdin, L. Mezeix, C. Bouvet, J. Morlier, and Y. Gourinat, "Fabrication and mechanical testing of glass fiber entangled sandwich beams: a comparison with honeycomb and foam sandwich beams", *Compos. Struct.* **90**:4 (2009), 404–412.

[Tian et al. 2007] J. Tian, T. J. Lu, H. P. Hodson, D. T. Queheillalt, and H. N. G. Wadley, "Cross flow heat exchange of textile cellular metal core sandwich panels", *Int. J. Heat Mass Transf.* **50**:13–14 (2007), 2521–2536.

[Vinson 1999] J. R. Vinson, *The behavior of sandwich structures of isotropic and composite materials*, Technomic, Lancaster, PA, 1999.

[Wadley et al. 2003] H. N. G. Wadley, N. A. Fleck, and A. G. Evans, "Fabrication and structural performance of periodic cellular metal sandwich structures", *Compos. Sci. Technol.* **63**:16 (2003), 2331–2343.

[Wadley et al. 2007] H. N. G. Wadley, K. P. Dharmasena, D. T. Queheillalt, Y. C. Chen, P. Dudt, D. Knight, K. Kiddy, Z. Xue, and A. Vaziri, "Dynamic compression of square honeycomb structures during underwater impulsive loading", *J. Mech. Mater. Struct.* **2**:10 (2007), 2025–2048.

[Wadley et al. 2013] H. N. G. Wadley, T. Børvik, L. Olovsson, J. J. Wetzel, K. P. Dharmasena, O. S. Hopperstad, V. S. Deshpande, and J. W. Hutchinson, "Deformation and fracture of impulsively loaded sandwich panels", *J. Mech. Phys. Solids* **61**:2 (2013), 674–699.

[Wei et al. 2008] Z. Wei, V. S. Deshpande, A. G. Evans, K. P. Dharmasena, D. T. Queheillalt, H. N. G. Wadley, Y. V. Murty, R. K. Elzey, P. Dudt, Y. C. Chen, D. Knight, and K. Kiddy, "The resistance of metallic plates to localized impulse", *J. Mech. Phys. Solids* **56**:5 (2008), 2074–2091.

[Xue and Hutchinson 2004] Z. Xue and J. W. Hutchinson, "A comparative study of impulse-resistant metal sandwich plates", *Int. J. Impact Eng.* **30**:10 (2004), 1283–1305.

[Zok et al. 2004] F. W. Zok, S. A. Waltner, Z. Wei, H. J. Rathbun, R. M. McMeeking, and A. G. Evans, "A protocol for characterizing the structural performance of metallic sandwich panels: application to pyramidal truss cores", *Int. J. Solids Struct.* **41**:22–23 (2004), 6249–6271.

[Zok et al. 2005] F. W. Zok, H. J. Rathbun, M. He, E. Ferri, C. Mercer, R. M. McMeeking, and A. G. Evans, "Structural performance of metallic sandwich panels with square honeycomb cores", *Philos. Mag.* **85**:26–27 (2005), 3207–3234.

RYAN L. HOLLOMAN: rlh5v@virginia.edu
Department of Materials Science and Engineering, University of Virginia, P.O. Box 400240, 351 McCormick Rd, Charlottesville, VA 22903-4240, United States

KARTHIKEYAN KANDAN: kk412@cam.ac.uk
Department of Engineering, Cambridge University, Trumpington Street, Cambridge, CB2 1PZ, United Kingdom

VIKRAM DESHPANDE: vsd20@cam.ac.uk
Department of Engineering, Cambridge University, Trumpington Street, Cambridge, CB2 1PZ, United Kingdom

HAYDN N. G. WADLEY: haydn@virginia.edu
Department of Materials Science and Engineering, University of Virginia, P.O. Box 400240, 351 McCormick Rd, Charlottesville, VA 22903-4240, United States

JOURNAL OF MECHANICS OF MATERIALS AND STRUCTURES

msp.org/jomms

Founded by Charles R. Steele and Marie-Louise Steele

Cover photo: Mando Gomez, www.mandolux.com

Journal of Mechanics of Materials and Structures